Azerbaijan Journal of Physics

Fizika

Azerbaijan Journal of Physics

FIZIKA

G.M. Abdullayev Institute of Physics
Azerbaijan National Academy of Sciences
Department of Physical, Mathematical and Technical Sciences

THE FORMATION OF SLIP BANDS IN LAYERED CRYSTALS

N.M. ABDULLAYEV[1], A.Sh. KAKHRAMANOV[2], K.G.KHALILOVA[1], S.R. AZIMOVA[1]

[1]*Institute of Physics of Azerbaijan NAS, Baku, Azerbaijan*
[2]*Baku State University, Baku, Azerbaijan*
abnadir@mail.ru

The formation of slip bands in $A^V B^{VI}$ foils is considered as dislocation process self-organization being in dislocation ensemble at level 10-20nm. The band distortion region in Bi_2Te_3 and Sb_2Te_3 basal planes are revealed.

Keywords: slip bands, layered crystal
PACS: 68.35.bj

INTRODUCTION

At plastic deformation of layered single crystals (non-homogeneously doped [1 -4]) it is revealed that the formation of slip lines and bands in them is sensitive to layer hardness. The band "splitting" on separate more narrow slip bands evidences about process of advanced deformation localization in hard layers in comparison with smooth ones.

In [3-5] it is also revealed that penetration of spiral bands in hard layers not always leads to band splitting (branching) on separate more narrow ones and can be accompanied by only effect of bandwidth reduction. The general uniform decrease of band width at its penetration in strong layer and also small gradual decrease of band width as far as this penetration [1] is accepted as effect of bandwidth reduction. This circumstance shows on the fact that localization and delocalization effects of deformation are connected with mobility of spiral dislocations in transversal direction to dislocation slip plane and ability of spiral dislocation to multiplication by double transversal slip the parameters of which are strongly depends on doping level [6,7].

As the formation of slip bands is the result of dislocation process self-organization developing in dislocation ensemble at meso-level [8], it is obvious that observable peculiarities of slip band formation in layered crystals should be explained within the framework of kinetic approach to these phenomena. The solution of this task is the aim of work [1]. The equations of dislocation density evolution are used.

DISLOCATION DENSITY. THE NARROWING EFFECTS OF SLIP AND BRANCHING BANDS.

The equations of density evolution of $p_m(x, y, t)$ mobile and $p, (x, y, t)$ immobile dislocations describing the formation of slip band lengthening in direction of **x-** axis and widening in direction of y-axis, have the form [1]:

$$t_m \frac{\partial \rho_m}{\partial t} = \left(R_x^{(m)}\right)^2 \frac{\partial^2 \rho_m}{\partial x^2} + \left(R_y^{(m)}\right)^2 \frac{\partial^2 \rho_m}{\partial y^2} + n\lambda_m + \rho_m - \beta\rho_i \tag{1}$$

$$\rho_i(x,y,t) = \left(R_x^i R_y^i\right)^{-1} \int_x^\infty e^{-\frac{|x-x'|}{R_x^{(i)}}} dx' \times \int_y^\infty e^{-\frac{|y-y'|}{R_y^{(i)}}} \rho_m(x',y',t) d \tag{2}$$

Here t is time, t_m —λ_m/u and λ_m are time and distance between dislocation multiplication acts and mechanism of double transversal slip of spiral dislocations correspondingly, u is dislocation velocity, n is density of dislocation sources by Frank-Reed type, β is relative coefficient of dislocation immobilization in dipoles. $R_{x,y}^{(m)}$ and $R_{x,y}^{(i)}$ parameters define the character self-organization scales of mobile and immobile dislocations at lengthening and widening of the band. They depend on kinetic coefficients defining the multiplication processes intensity, immobilization and dislocation diffusion [8]. The crystal doping strongly influences on kinetic coefficients [6,7] and consequently, on $R_{x,y}^{(m)}$ and $R_{x,y}^{(i)}$ parameters and their ratio that influences on slip band formation process.

The formation of slip bands and peculiarities of their formation in non-homogeneously strong (layered) crystals are connected with dislocation self-organization process.

The thin crystal foils $A^V_2B^{VI}_3$ are obtained by gradual (0001) surface peeling. The films by thickness from 10^3 nm up to 20nm are obtained by this way. The above mentioned is proved by process of growth and surface morphology of layered crystals on example of thin foils Sb_2Te_3 and Bi_2Te_3. The linear and planar defects of crystal structure and their electron-microscopic images are schematically shown in fig.1 on the base of results of series of experimental and theoretical works [9].
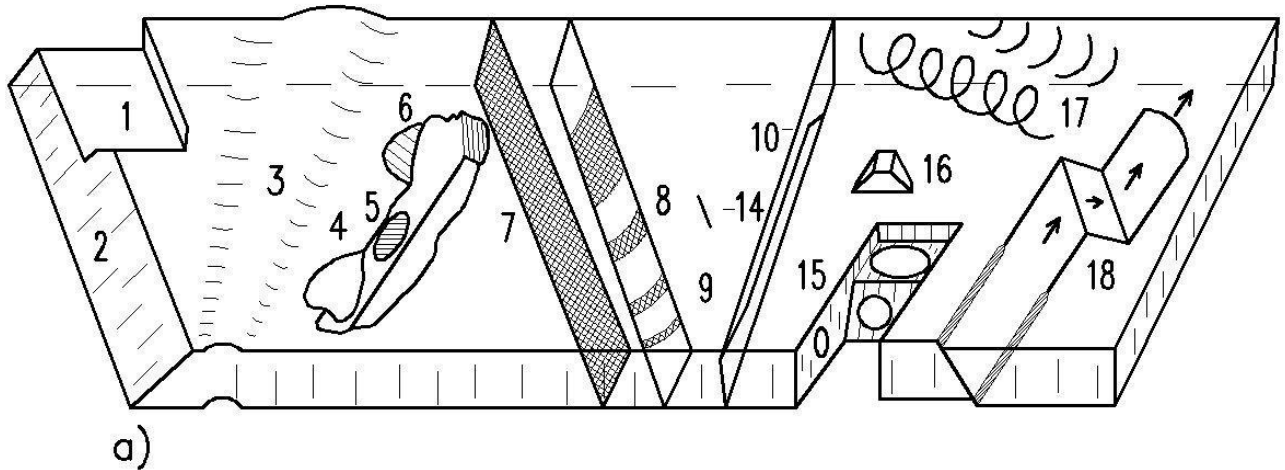
Fig.1.a. The foil with main defects.

1 - 6 - are heterogeneities of thickness or foil inclination; *7-18* are defects of crystal structure; *1* is decreased thickness region, *2* – foil taped edge, *3* is foil bend,4 *-5* are pores; *6* are nano-islands on the foil; *7* is package defect; *8* are splitted dislocations with package defect different thickness between partial dislocations; *9* is total (undissociated) dislocation, *10* is dislocation general type
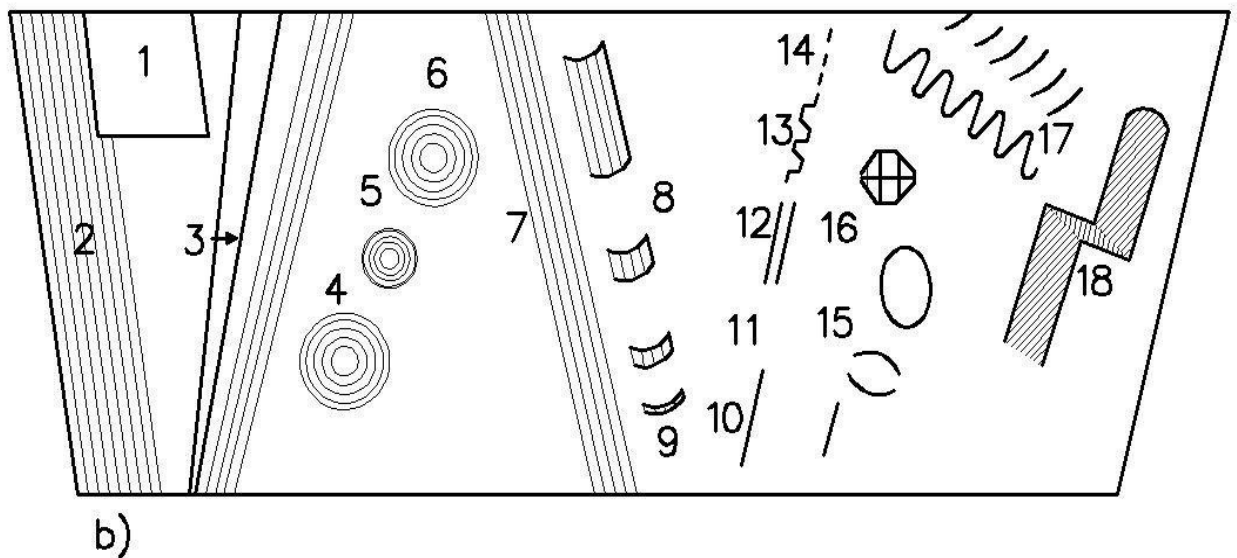
Electron image of defects

Fig.1.b. The scheme of metal foil image in transmission electron microscope, designations:
  10 - 14 is long dislocation; *11* is invisible dislocation; *12* is double image on which the different contrast effects are shown, *13* is zigzag, *14* is dotted line; *15* are dislocation loops differently situated in foil; *16* is packing defect tetrahedron; *17* are helicoidal dislocations; *18* is the track of previous dislocation with double transversal shift (arms show on the dislocation movement direction).

The forms of slip bands and regions with plates in basic plane of Sb_2Te_3 and Bi_2Te_3 crystals are experimentally revealed by us and scales of their decrease are observed (see fig.2 - 4).

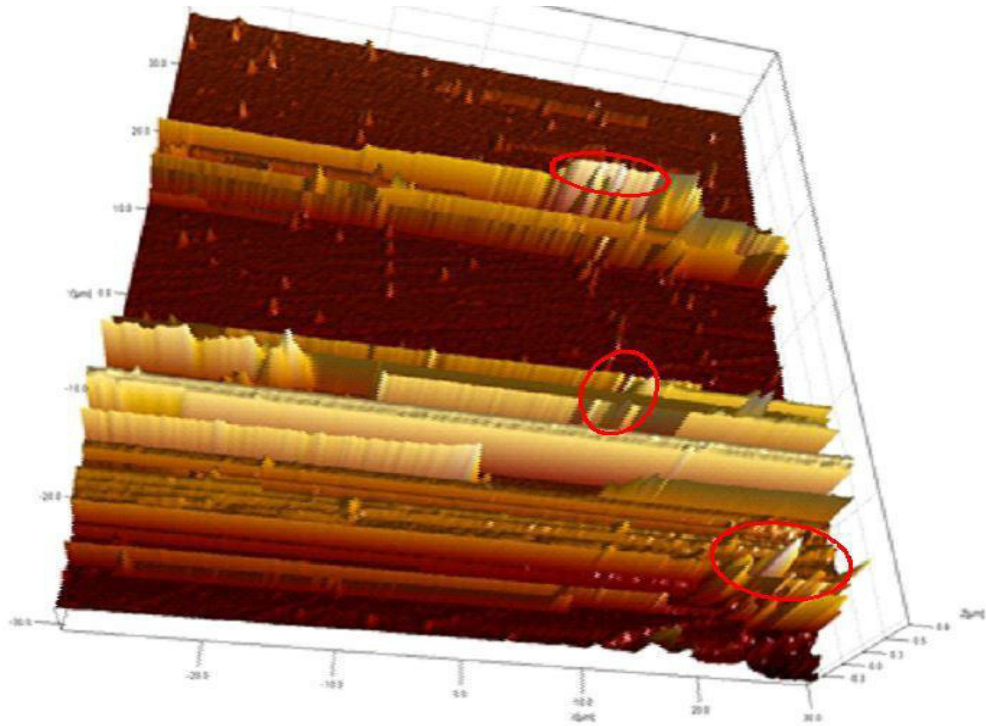*Fig.2.* The experimental form of slip band on surface (0001) Bi_2Te_3 doped by (In-Cu) forming the n-type region. The defect places of slip bands are shown by circles.
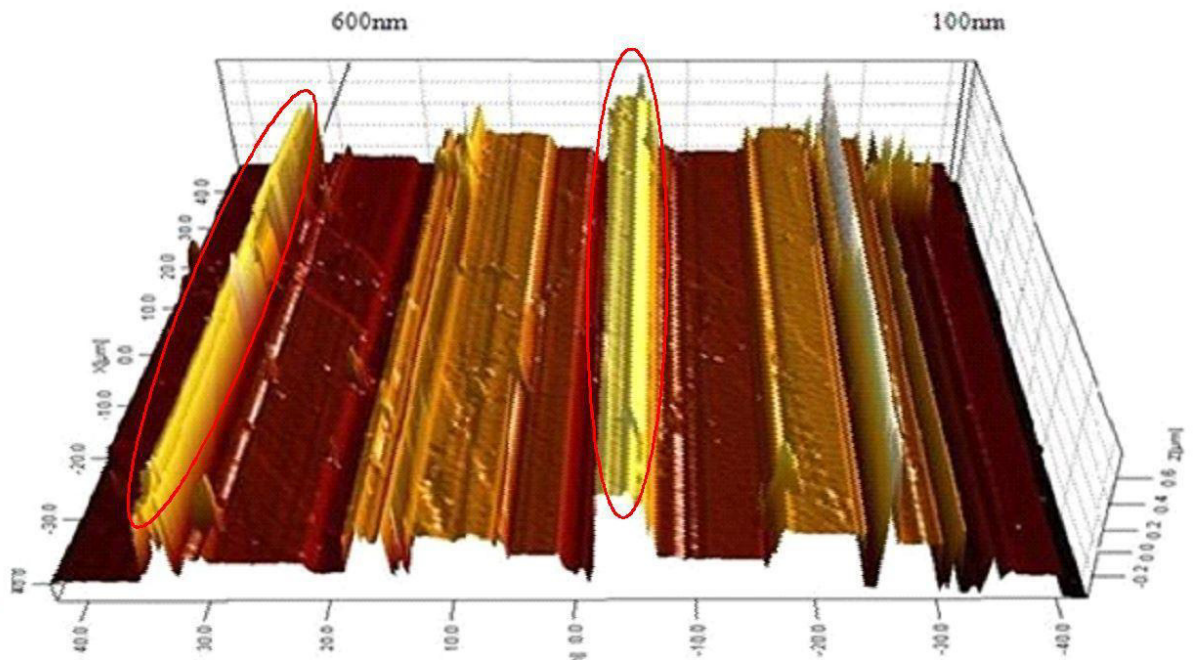

Fig.3. The stressed regions with plates in Sb_2Te_3 in basic plane (0001) in 3D-scale with decrease level.
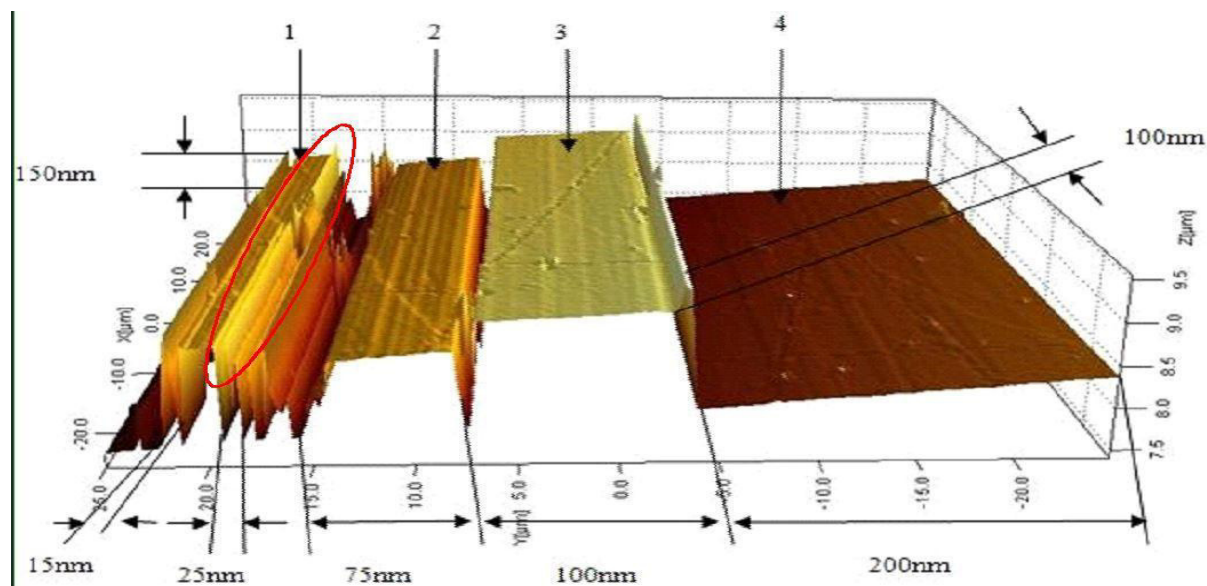
Fig.4. Sb$_2$Te$_3$ relief with decrease scale from 150 up to 100nm and dislocation width. Designations are: 1 is dislocation width 10-15nm; 2 is step plateau by size 75nm; 3 is step plateau 100nm, 4 is step plateau 200 nm.

The relief has the stepped character proving the process of branching self-organization in layered crystals. The regions of plateau and stresses between plateaux shown by ellipses are emphasized in fig.2 - 4.

The following conclusions are made on the base of equation analysis of density dislocation evolution with sample surface morphology.

CONCLUSIONS

$A^V B^{VI}$ foil surface including several structural levels by height from 150 up to 1,5nm is the one of peculiarities of slip bands. (0001) $A^V B^{VI}$ surfaces have the stepped plateau-like character proving the branching self-organization process in layered crystals by $A^V_2 B^{VI}_3$ type.

_____

[1] *Q.A. Maliqin.* FTT, 1999, tom 41, vip. 2, s.252-258. (In Russian).
[2] *A.V. Nikiforov, Yu.Q. Nosov, M.B. Muxamedjanova, O.V. Klyavin, P.I. Antonov.* FTT 29, 2, 485 (1987). (In Russian).
[3] *Q.V. Berejkova, N.P. Skvorchova, A.V. Nikiforov, Yu.Q. Nosov, V.R. Reqel, M.A. Chernisheva.* FTT 31, 2, 252 (1989). (In Russian).
[4] *A.V. Nikiforov, O.V. Klyavin.* FTT 38, 9, 2744 (1996). (In Russian).
[5] *B.I. Smirnov, T.S. Orlova.* FTT 38, 8, 2431 (1996). (In Russian).

[6] *B.I. Smirnov.* Dislokachionnaya struktura i uprochenie kristallov. Nauka, L. (1981). 232 s. (In Russian).
[7] O.V. Klyavin. Fiziki plastichnosti kristallov pri qelievix temperaturax. Nauka, M. (1987). 255 s. (In Russian).
[8] *Q.A. Maliqin.* FTT,37, 1, 3 (1995). (In Russian).
[9] *L.Q. Orlov, 31. P. Usikov, L.M. Utevskiy.* UFN, 1962 q. T. LXXVI, vip. 1, s. 109. (In Russian).

Recevied: 12.09.2018

SPECTRAL DENSITY OF THE ULTRA SHORT LASER PULSES AT PARAMETRIC INTERACTION IN METAMATERIALS

Sh.Sh. AMIROV [1,2], Z.H. TAGIYEV[1], G.N. AHMADOV[3]

[1] *Department of Medical Physics and Informatics , Azerbaijan Medical University,*
98 Mardanov qardashlari str., Az-1078 Baku, Azerbaijan ,
[2]*Department of Electronics ,Telecommunications and Radioengineering, Khazar University,*
41 Mahsati str., Az 1096 Baku, Azerbaijan
[3]*G.M.Abdullayev Institute of Physics of Azerbaijan NAS, H.Javid ave., 131, Baku , Azerbaijan*
e-mail: Shahmardan.amirov@khazar.org

A three -wave parametric interaction in metamaterials is analyzed via consideration the negative refraction at the frequency of a signal wave. Analytic expression for the spectral density of a backward signal wave is obtained in the presence of group velocity mismatch and group velocity dispersion. When characteristic lengths of group velocity mismatch and the group velocity dispersion are less than the nonlinear length the excited pulse splits into narrow peaks . It is shown that, at the ratio of characteristic lengths $l_{nl}/l_v = 0$, the graph of the spectral density is symmetric relatively negative and positive values of phase modulation parameter.

INTRODUCTION

The negative index materials (NIM) are attractive due to specifics of their interaction with electromagnetic waves [1,2]. Different signs of refractive index correspond to different frequency intervals of   the interacting waves. Therefore the energy fluxes (Poynting vector) of the waves with a positive sign of refractive index will propagate in opposite direction to those with frequencies corresponding to a negative sign of refractive index. . The dynamics of three wave interaction in NIM was considered   for the case of second harmonic generation in [3]. Results obtained in [4,5] are being used for the developments the metamaterials in the near IR and visible ranges of the spectrum. Earlier we have analyzed the efficiency of energy conversions between two direct waves with respect to the energy of the backward signal wave for the case of signal-wave amplification in metamaterials [6] in the constant intensity approximation (CIA) [7,8], taking into account the reverse reaction of excited wave on the exciting one. By employing the CIA we have studied the parametric interaction of optical waves in metamaterials under low-frequency pumping in the case of a negative index at a signal wave frequency [9] .The analytic expressions obtained in CIA showed , that the choice of the optimum parameters for the pump intensity, total length of the metamaterial and phase mismatch   will facilitate obtaining the regimes of an effective amplification as well as the generation of signal wave. The characteristic processes observed at parametric interactions   of   running   and   counter   waves   in metamaterials are the transition processes [10]. Authors [11,12,13] were analyzed the transition processes by employment the first order dispersion theory in the medium with quadratic nonlinearity. In case of counter waves the phase matching condition is executed due to opposite directionality of the Poynting vector to the wave vector. To pump the nonlinear crystal of parametrical amplifier the nanosecond pulses of laser radiation are

required. Parametric amplification of light in nonlinear crystals can be used for amplification the radiation being used with the aim of optical stochastic cooling of the relativistic heavy ions [14] Note that earlier we have employed constant intensity approximation to study the stationary optical parametric amplification [15] in the Fabri-Perrot cavity filled with dissipative dispersive nonlinear medium. Here optimization of various parameters such as the length of the nonlinear medium, wave mismatch, intensities of the pump and idler waves were considered to maximize the signal wave gain.

Under reduction in the pulse duration the character of interaction of modulated wave significantly depends on the dispersion properties of a medium. The frequency conversion for the ultra-short pulses with running wave was analyzed in [16]. Note that the growing interest to the non-stationary interaction of ultra-short pulses of light in nonlinear medium is related to the development of powerful sources of light pulses of femtosecond duration [1]. Earlier in [17] we were studied influence of group velocity mismatch (GVM) as well as group velocity dispersion (GVD) to the generation of sum frequency of ultra- short pulses in an external cavity under the phase matching and absence of linear losses . It was shown that in some cases efficiency of conversion in the existence of GVM and GVD can be significantly higher as compared as to the absence of mismatch and dispersion using the Gaussian pulse with quadratic phase modulation as the input pulse led to compression of spectrum with increase in GVM and decrease in GVD. It was obtained that maximum energy of conversion is reached not at group phase matching, but at the definite characteristic lengths of GVM and GVD.

2. DISCUSSIONS AND RESULTS

In the present work we investigate theoretically the non-stationary parametric amplification in metamaterials in the second order dispersion theory. We study this

problem assuming that the nonlinear crystal has length l, and its cross section is much larger than the input laser beam. We ignore any reflections at the crystal surfaces. The beam axis (which we term) is normal to the crystal surface, and this is the direction of the input wave vector. The input surface of the crystal is at $z = l$. We assume for definiteness that for a parametric three-wave interaction in a metamaterials the medium is "left" at the frequency of the signal wave only. Here the pump wave is a long pump pulse with frequency ω_3 an idler wave is at frequency ω_2 and a signal wave is at the difference frequency $\omega_1 = \omega_3 - \omega_2$. The geometry of the problem is so that the pump and idler waves enter the nonlinear medium from the left $(z = 0)$, but the signal wave from the right $(z = l)$ hand side. In such a consideration the wave vectors of all interacting waves in a metamaterial propagate in the positive direction of the z axis. During the wave propagation in a nonlinear medium as a result of the nonlinear interaction the energy exchange occurs between the counter wave packets of two types : direct waves (the idler and pump waves) and an backward wave (the signal wave); this leads to the energy transfer from the pump and idler waves into the signal-wave energy. For the negative values of the dielectric permittivity and magnetic permeability at the signal wave frequency ω_1 and the positive values at the frequencies ω_2, ω_3 the parametrical interaction is described by the system of parametrically coupled equations [1].

$$\left(\frac{\partial}{\partial z} + \frac{1}{u_1}\frac{\partial}{\partial t} - i\frac{g_1}{2}\frac{\partial^2}{\partial t^2} + \delta_1\right)A_1 = -i\gamma_1 A_3 A_2^* e^{i\Delta z}$$

$$\left(\frac{\partial}{\partial z} + \frac{1}{u_2}\frac{\partial}{\partial t} - i\frac{g_2}{2}\frac{\partial^2}{\partial t^2} + \delta_2\right)A_2 = -i\gamma_2 A_3 A_1^* e^{i\Delta z} \quad (1)$$

$$\left(\frac{\partial}{\partial z} + \frac{1}{u_3}\frac{\partial}{\partial t} - i\frac{g_3}{2}\frac{\partial^2}{\partial t^2} + \delta_1\right)A_3 = -i\gamma_3 A_1 A_2 e^{-i\Delta z}$$

here A_j (j=1-3) are the corresponding complex amplitudes of the signal, idler and pump waves

respectively, δ_j are the absorption coefficients of the medium at frequencies ω_j (j=1-3), u_j are the group velocities of the interacting waves, $\Delta = k_1 - k_2 - k_3$ is the phase mismatch between the interacting waves, $g_j = \partial^2 k_j / \partial \omega_j^2$ (the 3-rd term in the Taylor expansion around the central frequency $\omega_0: \Delta\omega = \omega - \omega_0$, $k_n(\omega) \cong k_n(\omega_0) + k_n'\Delta\omega + \frac{1}{2}k_n''\Delta\omega^2 + \cdots$) is the dispersion of group velocities and γ_1, γ_2, γ_3, are the coefficients of nonlinear coupling

$$\gamma_1 = = \frac{8\pi\chi_{eff}^2 \omega_1^2|\varepsilon_1|}{k_1 c^2}, \qquad \gamma_2 = \frac{8\pi\chi_{eff}^2 \omega_2^2\varepsilon_2}{k_2 c^2},$$

$$\gamma_3 = \frac{8\pi\chi_{eff}^2 \omega_3^2\varepsilon_3}{k_3 c^2},$$

where χ_{eff}^2 is the effective quadratic susceptibility of the medium.

Assuming pump wave amplitude to be constant ($A_3 = A_{30} = const.$) and having put substitution $\eta = t - \frac{z}{u_1}$ the set of above equations (1) is reduced to

$$\left(\frac{\partial}{\partial z} - i\frac{g_1}{2}\frac{\partial^2}{\partial \eta^2} + \delta_1\right)A_1(z, \eta) = -i\gamma_1 A_{30} A_2^*(z, \eta)e^{i\Delta z}$$

$$\left(\frac{\partial}{\partial z} + v\frac{\partial}{\partial \eta} - i\frac{g_2}{2}\frac{\partial^2}{\partial \eta^2} + \delta_2\right)A_2(z, \eta) =$$
$$-i\gamma_2 A_{30} A_1^*(z, \eta)e^{i\Delta z} \qquad (2)$$

where $v = 1/u_2 - 1/u_1$ is a group velocity mismatch. To analyze the system (2) it is convenient to use the Fourier transformation

$$A_{1,2}(z, \eta) = \int_{-\infty}^{+\infty} A_{1,2}(z, \omega)e^{-i\omega\eta}d\omega \qquad (3)$$

Substituting (3) into (2) yields

$$\left(\frac{\partial}{\partial z} + i\frac{g_1}{2}\omega^2 + \delta_1\right)A_1(z, \omega) = -i\gamma_1 A_{30} A_2^*(z, \omega)e^{i(\omega\eta + \Delta z)}$$
$$\left(\frac{\partial}{\partial z} + i\frac{g_2}{2}\omega^2 - iv\omega + \delta_2\right)A_2(z, \omega) = -i\gamma_2 A_{30} A_1^*(z, \omega)e^{i(\omega\eta + \Delta z)} \qquad (4)$$

Solving this system in the absence of losses ($\delta_i = 0$) gives following expression for the amplitude of a signal wave

$$A_1(\omega, z) = \frac{i\gamma_1 A_{30} A_2}{\lambda - k\tan\lambda\, l}(\cos\lambda z \cdot \tan\lambda l - \sin\lambda z)e^{-kz} \qquad (7)$$

where $\lambda = l_{nl}^{-1} \left[\left(\frac{1}{4}\frac{l_{nl}}{l_d}(\alpha + 1)\omega^2\tau^2 - \frac{1}{2}\frac{l_{nl}}{l_v}\omega\tau + \frac{\Delta}{\Gamma_3}\right)^2 - 1\right]^{1/2}$,

$k = l_{nl}^{-1}[i(\frac{1}{4}(\alpha - 1)\frac{l_{nl}}{l_d}\omega^2\tau^2 - \frac{l_{nl}}{l_v}\omega\tau + \frac{\Delta}{\Gamma_3})]$, $\quad \alpha = \frac{g_2}{g_1}$, $l_d = \frac{\tau^2}{g_1}$, $l_v = \frac{\tau}{v}$

Furthermore we assume that the input wave is Gaussian with a quadratic phase modulation .

$$A_2(t) = A_{20}e^{-\frac{t^2}{2\tau^2} - i\gamma\frac{t^2}{2}} \qquad (8)$$

Using the Fourier transformation

$$A_2(\omega) = \frac{A_{20}}{2\pi}\int_{-\infty}^{+\infty} e^{-\frac{t^2}{2\tau^2} - i\gamma\frac{t^2}{2}}e^{-i\omega t}dt \qquad (9)$$

for the spectral density we obtain the following expression

$$S_2(\omega) = \frac{A_{20}\tau^2}{2\pi} \frac{1}{\sqrt{1+p}} e^{-\frac{\mu^2}{1+p}} \tag{10}$$

where $\quad p = \gamma^2\tau^4 \quad$ and $\quad \mu = \omega\tau$ are the frequency modulation and phase modulation parameters respectively. Substituting (9) into (7) for spectral density of a signal wave $S_1(\omega, z) = A_1(\omega, z) \cdot A_1^*(\omega, z)$ has resulted

$$S_1(\omega, z) = K \frac{e^{-\frac{\mu^2}{1+p}}(tan\lambda l \cdot cos\lambda z - sin\lambda z)^2}{(\lambda z)^2 + (kz)^2 tan^2\lambda l} \tag{11}$$

where $\quad K = \frac{cn\gamma_1^2 I_{30} I_{20}\tau^2 z^2}{16\pi}$

From (11) it follows that the shape of a spectrum of a amplified signal wave is determined not only by the values of z, l_{nl}, l_v and l_d but also with their quotients z/l_{nl}, l_{nl}/l_v, l_{nl}/l_d. In Fig. 1 the dependences of a spectral density $S_1(\omega, z)$ on the phase modulation parameter $\omega\tau$ are illustrated at different values of l_{nl}/l_v and l_{nl}/l_d. As can be seen, the shape of a spectrum varies with the change in these ratios, in particular, when $l_{nl}/l_v = 0$ (curves 1 and 3), the spectrum becomes symmetric relatively negative and positive values of phase modulation parameter.
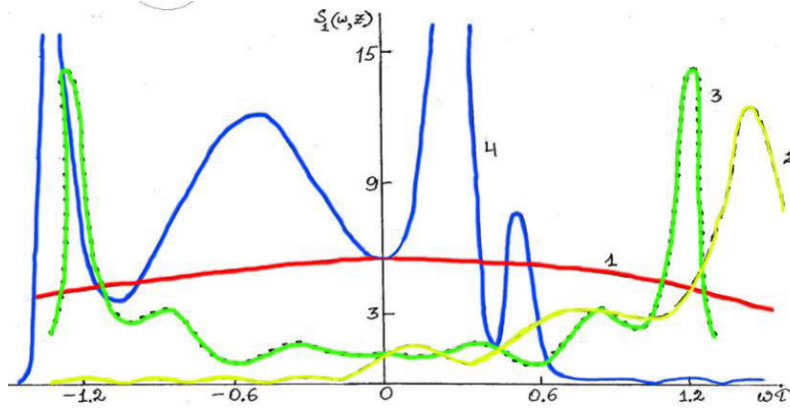

Fig. 1. The reduced spectral density $S_1(\omega, z)$ of a signal wave versus phase modulation parameter $\omega\tau$ for $p = 5$, $z / l_{nl} = 0,5$, $\Delta = 0, \delta_i = 0$: $1 - l_{nl}/l_v = l_{nl}/l_d = 0$; $2 - l_{nl}/l_v = 3$, $l_{nl}/l_d = 0$; $3 - l_{nl}/l_v = 0$, $l_{nl}/l_d = 3$; $4 - l_{nl}/l_v = l_{nl}/l_d = 3$

In Fig. 2 a spectral density is given as a function of phase modulation at different values of intensity of idler wave. As can be seen at the same values of input intensity (curves 1 and 2) increase in frequency modulation leads to increase in spectral density, however at equal frequency modulations increase in intensity decreases the spectral density of an amplified signal wave (curves 1 and 3).

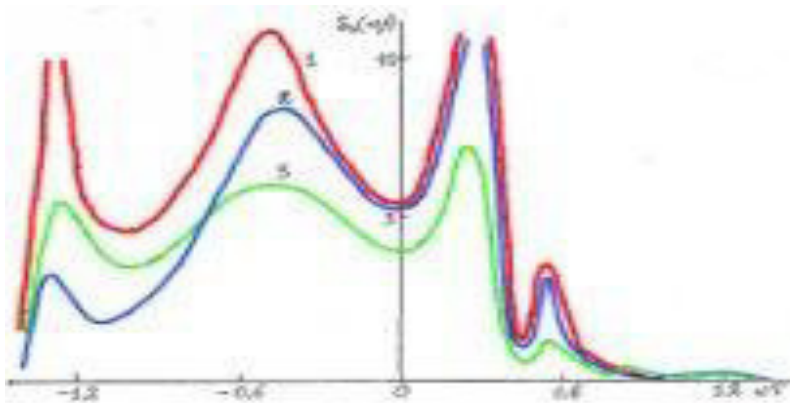*Fig. 2.* The reduced spectral density $S_1(\omega, z)$ of a signal wave as a function of phase modulation parameter $\omega\tau$ for $z / l_{nl} = 0,7$ (curves 1 and 2) and $z/l_{nl} = 1$ (curve 3), $p = 0$(curve 2), $p = 5$ (curves 1 and 3) and $\Delta = 0, \delta_i = 0$

Effect of phase modulation of idler wave onto the spectral density of amplified signal wave also is demonstrated in Fig .3.
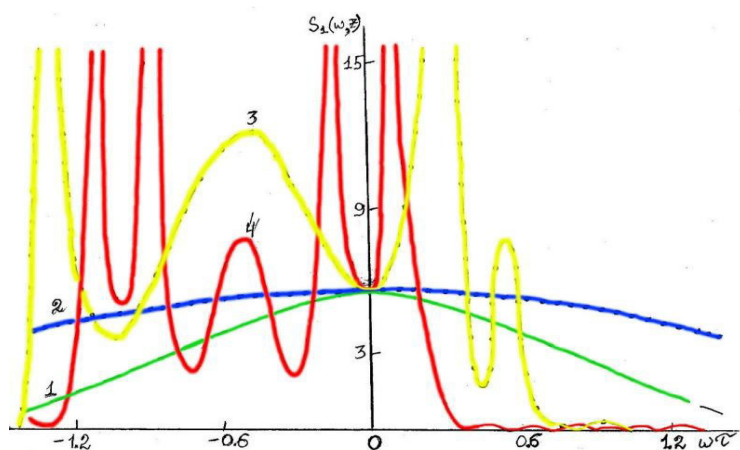
Fig. 3. Dependences of a spectral density $S_1(\omega, z)$ of a signal wave on the phase modulation parameter $\omega\tau$ for $p = 0$ (curve 1), $p = 5$ (curves $2 - 4$) and $z / l_{nl} = 0.5$, $\Delta = 0$, $\delta_i = 0$ at different values of ratios of characteristic lengths: $1 - l_{nl}/l_v = l_{nl}/l_d = 0$; $2 - l_{nl}/l_v = l_{nl}/l_d = 0$; $3 - l_{nl}/l_v = l_{nl}/l_d = 3$; $4 - l_{nl}/l_v = l_{nl}/l_d = 10$;

From Fig. 3 it is seen that, a spectrum is symmetric when $l_{nl}/l_v = 0$ independently on the value of l_{nl}/l_d . Existence of phase modulation leads to increase in the width of spectrum of a signal wave. At larger values of a frequency modulation ($\gamma\tau^2 \gg 1$) the splitting up occurs in the spectral density of amplified pulse (curve 4) . All curves in Fig. 1-3 are plotted for the same signs of the coefficients of group velocity dispersions. Note that when $g_1 = g_2$, amplification of signal wave occurs without dispersion of group velocities. The graphs are plotted for the case when $g_2/g_1 = 3$.

CONCLUSION

From above mentioned one can conclude that parametric amplification of ultra-short pulses in metamaterial in the second order dispersion theory is affected by the influence of group velocity mismatch as well as the group velocity delay .

Here an analytical expressions for the spectral density of a signal wave was derived . We showed that the spectral density of a ultra-short pulse wave is affected by the ratios of characteristic lengths. When $l_{nl}/l_v = 0$, the shape of a graph of the spectral density becomes symmetric relatively negative and positive values of phase modulation parameters and has a maximum at positive values of phase modulation when $l_{nl}/l_d = 0$.

For the ratios of characteristic lengths differ from zero maxima of spectral density are obtained not at zero $\omega\tau$ but at different values of this parameter.

_____

[1] *S.A. Akhmanov and R.V. Khokhlov.* Ah. Eksp. Teor. Fiz. 43, 351 (1962) [Sov. Phys. JETP 16, 252, (1963)]

[2] *S.A. Akhmanov, V.A. Visloukh, A.S. Chirkin.* UFN 1986 , v. 149, issue 3, p.449-509.

[3] *A.I. Maimistov, I.R. Gabitov and E.V.Kazantseva.* Opt. Spectrosk., 102, p. 99 (2007) [Opt. Spectros. (Eng.Transl.), 102, p.90]

[4] *S. Zhang et al.* Phys. Rev. Lett., 95 (2005).

[5] *W. Cai, V.M. Shalaev.* Optical Metamaterials, Fundamentals and Applications (New York, Springer, 2010).

[6] *R.J. Kasumova, Z.H. Tagiev, Sh.Sh. Amirov, Sh.A. Shamilova and G.A. Safarova.* Journal of Russian Laser Research, Vol. 38, No. 4, p.211-218.

[7] *Z.H. Tagiev, A.S. Chirkin.* Sov.Phys. JETP, 46, 669 (1977) [Zh. Eksp. Teor.Fiz. 73, 1271 (1977)*; Z.H. Tagiev, R.J. Kasumova, R.A. Salmanova, N.V. Kerimova.* J.Opt B., 3, 84 (2001).

[8] *V.G. Dmitriev, L.V. Tarasov.* Prikladnayanelineynayaoptika (Applied Nonlinear Optics) (Moscow, Fizmatgiz, 2004), p.352.

[9] *R.J. Kasumova, Sh.Sh. Amirov, Sh.A. Shamilova.* Quantum Electronics 47 (7) p.655-660 (2017).

[10] *V.V. Slabco, A.K. Popov, C.A. Myslivets, E.V. Rasskazova, V.A. Tkachenko.* KvantovayaElectronika 45, No 12 p.1151-1152 (2015).

[11] *A.K. Popov, V.M. Shalaev.* Appl.Phys. B, 84 131 (2006).

[12] *M.I. Shalaev, S.A. Myslivets et al.* Opt. Lett., 36, 3861 (2011).

[13] *I.V. Shadrirov, A.A. Zharov, Y.S. Kivshar.* J.Opt.Soc.Am.,B, 23, 529 (2006).

[14] *A. Piskarskas, A. Stabinis, A. Yankauskas.* UFN 1986 , v.150, issue 1, p. 127-143.

[15] *Z.A. Tagiev, Sh.Sh. Amirov.* Sov. J. Quantum Electron. 1989 (11) p.1442-1445.

[16] *S.A. Akhmanov, V.A. Visloukh, A.S. Chirkin.* UFN 1986 , v. 149, issue 3, p.449-509.

[17] *Sh.Sh. Amirov, Z.A. Tagiev.* Optika i SpektroskopiyaV.69, issue 3, p.678-683 (1990).

THE PRODUCTION OF HİGGS BOSON AND HEAVY FERMION PAIR IN ELECTRON-POSITRON COLLISIONS

S.K. ABDULLAYEV[1,a], M.Sh. GOJAYEV[1, b]

[1,2]*Baku State University*, *Faculty of Physics*, *Department of Theoretical Physics*,
Azerbaijan. *AZ* 1148, *Baku, Acad. Z. Khalilov*, 23
e-mail: [a]*s_abdullayev@bsu.edu.az,* [b]*m_qocayev@mail.ru*

Taking into account the arbitrary polarizations of the electron-positron pair and longitudinal polarizations of the fermionic pair, the differential cross sections of the Higgs boson and the heavy fermion pair production in electron-positron annihilation are calculated: $e^-e^+ \to H_{SM} f\bar{f}$, $e^-e^+ \to Hf\bar{f}$, $e^-e^+ \to hf\bar{f}$ and $e^-e^+ \to Af\bar{f}$. Characteristic features of the behavior of the cross sections, angular and spin correlations are investigated as a function of the scaling energies and the emission angles of the particles.

INTRODUCTION

The Standard Model (SM), based on a gauge theory with a symmetry group $SU(3)_C \times SU(2)_L \times U(1)$, quantitatively describes the physics of strong, electromagnetic, and weak interactions between leptons and quarks [1, 2]. In physics of elementary particles, no experiments have yet been observed, the results of which do not agree with the SM. Recently opened nedostayuschy brick in the building SM. This is a scalar Higgs boson, discoveries by ATLAS and CMS collaborations [3, 4] in the Large Hadron Collider (LHC). The discovery of the Higgs boson has experimentally confirmed the theoretically predicted mechanism of mass generation of fundamental particles – the mechanism of spontaneous Breit-Englert-Higgs symmetry breaking [5].

In the first experiments conducted in the LHC, the main properties of this particle are established: the Higgs boson is a scalar particle with a positive parity, a nonvanishing vacuum value of about 125 GeV, interacting with $W^\pm$- and Z^0-bosons with a constant proportional to their masses. With the discovery of Higgs boson, SM entered a new stage in the study of the properties of fundamental interactions of elementary particles. In this connection, interest in various channels for the production and decay of the Higgs boson has greatly increased [6-12].

We note that the collision of high-energy electrons and positrons is an effective method for studying the mechanisms of interaction of elementary particles. This is mainly due to two reasons. First, the interaction of electrons and positrons is described by the electroweak theory, and therefore the results obtained are well interpreted. Secondly, electrons and positrons do not participate in strong interactions, as a result of which the background conditions of experiments are substantially improved in comparison with the studies carried out with beams of hadrons. At present, electron-positron colliders of high energies are designed to study the physical properties of Higgs bosons: ILC, CLIC, FCC [13, 14], as well as muon colliders [15].

In a recent paper [10], we investigated the production of the Higgs boson and light fermion pair in arbitrarily polarized electron-positron collisions. In this paper we discuss the processes of the joint production of a Higgs boson and a longitudinally polarized heavy fermion pair in arbitrarily polarized electron-positron beams:

$$e^- + e^+ \to H_{SM} + f + \bar{f}, \qquad (1)$$

where $f\bar{f}$ it can be a lepton $\tau^-\tau^+$-pair or a $b\bar{b}$-, $t\bar{t}$-quark pair

1. Calculation of the square of the matrix element

We assume that in a e^-e^+-collision a heavy fermion pair is produced by an electromagnetic mechanism, and then a scalar Higgs boson H_{SM} is braked by the fermion and antifermion (see Fig. 1, where Feynman diagrams are illustrated, in the diagrams, 4-particle impulses are written in parentheses).
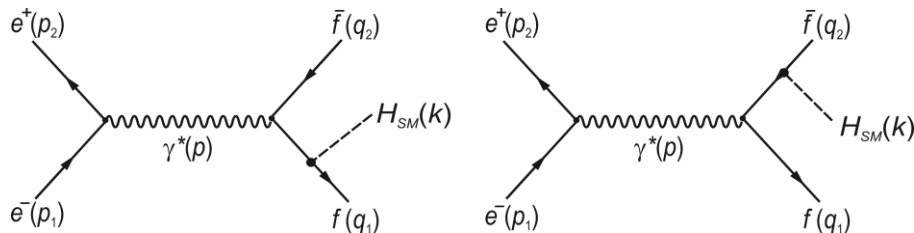

Fig. 1. Feynman diagrams of the process $e^-e^+ \to H_{SM} f\bar{f}$

Note that this reaction can occur due to a weak mechanism $e^- + e^+ \rightarrow (Z^*) \rightarrow H_{SM} + f + \bar{f}$, however, this mechanism is not considered here.

The following matrix element corresponds to the diagrams given:

$$M_{i \rightarrow f} = \frac{e^2 Q_f}{s} g_{H_{SM} f \bar{f}} \cdot [\bar{\upsilon}(p_2) \gamma_\mu u(p_1)] \cdot J_\mu, \tag{2}$$

where

$$J_\mu = \bar{u}_f(q_1) \left[\frac{\hat{q}_1 + \hat{k} + m_f}{(q_1 + k)^2 - m_f^2} \gamma_\mu - \gamma_\mu \frac{\hat{q}_2 + \hat{k} - m_f}{(q_2 + k)^2 - m_f^2} \right] \upsilon_f(q_2) \tag{3}$$

is fermionic electromagnetic current, $s = p^2 = (p_1 + p_2)^2$ – the square of the total energy of the electron and positron in the center of mass system, m_f and Q_f are the mass and electric charge of the fermion correspondingly, $g_{H_{SM} f \bar{f}}$ is the constant of the Higgs interaction of the boson with the fermion pair. According to the SM, this constant is proportional to the mass of the fermion

$$g_{H_{SM} f f} = \frac{m_f}{\eta} = m_f [\sqrt{2} G_f]^{1/2}.$$

Here $\eta = 246$ GeV is the vacuum value of the Higgs bosonic field, G_F is the Fermi constant of weak interactions.

The square of the matrix element (2) is expressed by the formula

$$|M_{i \rightarrow f}|^2 = \frac{e^4 Q_f^2}{s^2} g_{H_{SM} f f}^2 L_{\mu \nu} H_{\mu \nu}. \tag{4}$$

Here $L_{\mu \nu}$ and $H_{\mu \nu}$ are the conserved lepton and fermionic tensors

$$L_{\mu \nu} p_\mu = L_{\mu \nu} p_\nu = H_{\mu \nu} p_\mu = H_{\mu \nu} p_\nu = 0.$$

As a result, in the center-of-mass system, only the spatial components of these tensors contribute to the cross section:

$$L_{\mu \nu} H_{\mu \nu} = L_{mr} H_{mr} \quad (m, r = 1, 2, 3).$$

The tensor L_{mr} can easily be calculated on the basis of the matrix element (2), and in the case of annihilation of an arbitrarily polarized $e^- e^+$-pair, the structure has the following structure [16]:

$$L_{mr} = 2s[(1 - \lambda_1 \lambda_2)(\delta_{mr} - N_m N_r) + i(\lambda_2 - \lambda_1) \varepsilon_{mrs} N_s + \eta_{1m} \eta_{2r} + \eta_{1r} \eta_{2m} - (\vec{\eta}_1 \vec{\eta}_2)(\delta_{mr} - N_m N_r)], \tag{5}$$

where λ_1 and λ_2 ($\vec{\eta}_1$ and $\vec{\eta}_2$) are the helicities (transverse components of the spin vectors) of the electron and the positron, $\vec{N}$ is a unit vector directed along the momentum of the electron.

As for the fermionic tensor H_{mr}, we note that in the general case it is cumbersome and is therefore not given here. However, at high energies of the colliding particles ($\sqrt{s} \geq 1$ TeV), the ratio $\frac{m_f^2}{s}$ can be neglected in comparison with unity (for example, for the heaviest t-quark with a mass of 173.1 GeV, this ratio for $\sqrt{s} = 1$ TeV is $\left(\frac{173,1}{10^3}\right)^2 = 0,03 \ll 1$). Then, neglecting the terms proportional to $\frac{m_f^2}{s}$ and $\frac{M_{H_{SM}}^2}{s}$, we have a simple expression for the fermionic tensor (the fermions are longitudinally polarized):

$$H_{mr} = \frac{x_H^2}{2 x_{12}} [(1 + h_1 h_2)(\delta_{mr} - n_m n_r) - i(h_1 + h_2) \varepsilon_{mrs} n_s], \tag{6}$$

12

where $x_{12} = (1-x_1)(1-x_2)$, $x_1 = \dfrac{2E_1}{\sqrt{s}}$, $x_2 = \dfrac{2E_2}{\sqrt{s}}$ and $x_H = \dfrac{2E_H}{\sqrt{s}}$ are the scaling energies of the fermion, antifermion and Higgs boson, respectively, h_1 and h_2 are the helicities of the fermion and antifermion, $\vec{n}$ is the unit vector along the Higgs momentum of the boson.

The product of the lepton and fermion tensors can be represented in the form:

$$L_{mr} \cdot H_{mr} = \frac{1}{2}(L_{11} + L_{22}) \cdot \sigma_1 + (L_{22} - L_{11}) \cdot \sigma_2 + L_{33} \cdot \sigma_3 + (L_{13} + L_{31}) \cdot \sigma_4 - (L_{23} + L_{32}) \cdot \sigma_5 -$$

$$- (L_{12} + L_{21}) \cdot \sigma_6 - \frac{i}{2}(L_{12} - L_{21}) \cdot \sigma_7 - i(L_{23} - L_{32}) \cdot \sigma_8 - i(L_{31} - L_{13}) \cdot \sigma_9, \tag{7}$$

where the so-called correlation functions are introduced $\sigma_a\ (a = 1 \div 9)$, by means of relations:

$$\sigma_1 = H_{11} + H_{22}, \qquad \sigma_2 = \frac{1}{2}(H_{22} - H_{11}), \qquad \sigma_3 = H_{33},$$

$$\sigma_4 = -\frac{1}{2}(H_{13} + H_{31}), \quad \sigma_5 = -\frac{1}{2}(H_{23} + H_{32}), \quad \sigma_6 = -\frac{1}{2}(H_{12} + H_{21}), \tag{8}$$

$$\sigma_7 = i(H_{12} - H_{21}), \qquad \sigma_8 = \frac{i}{2}(H_{23} - H_{32}), \qquad \sigma_9 = \frac{i}{2}(H_{31} - H_{13}).$$

We use the coordinate system in which the OXZ plane coincides with the plane of particle production $\vec{q}_1 + \vec{q}_2 + \vec{k} = 0$ and introduce the angles θ, χ and φ, where θ is the polar angle between the Z axis and the direction of the electron beam, χ — the azimuth angle between the production plane and the plane determined by the Z axis and the beam e^-, φ is the azimuth angle between the production planes and transverse polarization of the electron. In this system, the components of the vectors $\vec{N}$, $\vec{\eta}_1$ and $\vec{\eta}_2$ is determined by expressions

$$\vec{N} = (\sin\theta \cdot \cos\chi,\ \sin\theta \cdot \sin\chi, \cos\theta),$$
$$\vec{\eta}_1 = -\vec{\eta}_2 = (-\sin\theta \sin\chi \cos\varphi - \cos\chi \sin\varphi,\ -\cos\theta \sin\theta \cos\varphi - \cos\chi \sin\varphi,\ \sin\theta \cos\varphi). \tag{9}$$

Then for the product of tensors $L_{mr} \cdot H_{mr}$ we have:

$$L_{mr} \cdot H_{mr} = 2s(1 + h_1 h_2)\left\{ \frac{1}{2}[(1 - \lambda_1\lambda_2)(1 + \cos^2\theta) + \eta_1\eta_2 \sin^2\theta \cos 2\varphi]\sigma_1 + \right.$$

$$+ [(1 - \lambda_1\lambda_2) \sin^2\theta \cos 2\chi - \eta_1\eta_2((1 + \cos^2\theta)\cos 2\chi \cos 2\varphi - 2\sin\theta \sin\chi \sin 2\varphi)]\sigma_2 +$$

$$+ [(1 - \lambda_1\lambda_2)\sin^2\theta - \eta_1\eta_2 \sin^2\theta \cos 2\varphi]\sigma_3 + [(1 - \lambda_1\lambda_2)\sin^2\theta \cos 2\chi + \eta_1\eta_2((1 + \cos^2\theta) \times$$

$$\times \sin 2\chi \cos 2\varphi + 2\cos\theta \cos 2\chi \sin 2\varphi)]\sigma_4 + [(1 - \lambda_1\lambda_2)\sin 2\theta \sin\chi -$$

$$- \eta_1\eta_2(\sin 2\theta \sin\chi \cos 2\varphi + 2\sin\theta \cos\chi \sin 2\varphi)]\sigma_5 +$$

$$\left. + [-(1 - \lambda_1\lambda_2)\sin 2\theta \cos\chi - \eta_1\eta_2(\sin 2\theta \cos\chi \cos 2\varphi - 2\sin\theta \sin\chi \sin 2\varphi)]\sigma_6 \right\} -$$

$$- 2s(h_1 + h_2)(\lambda_1 - \lambda_2)[\cos\theta \cdot \sigma_7 + 2\sin\theta(\cos\chi \cdot \sigma_8 + \sin\chi \cdot \sigma_9)]. \tag{10}$$

2. Differential cross section of the reaction $e^- e^+ \to H_{SM} f\,\bar{f}$

Based on the general rules for the differential cross section of the process $e^- + e^+ \to H_{SM} + f + \bar{f}$, the following expression is obtained

$$\frac{d^5\sigma}{d\chi d\varphi d(\cos\theta) dx_1 dx_2} = \frac{\alpha^2_{KED} Q_f^2 N_C}{256\pi^3 s}\, g^2_{H_{SM}ff} \{(1 + h_1 h_2)[(1 - \lambda_1\lambda_2)\sigma_A +$$

$$+\eta_1\eta_2(\cos 2\varphi\cdot\sigma_B-\sin 2\varphi\cdot\sigma_C)]+(\lambda_1-\lambda_2)(h_1+h_2)\sigma_D\}. \tag{11}$$

Here

$$\sigma_A=\frac{1}{2}(1+\cos^2\theta)\sigma_1+\sin^2\theta(\cos 2\chi\cdot\sigma_2+\sigma_3+\sin 2\chi\cdot\sigma_4)+\sin 2\theta(\sin\chi\cdot\sigma_5+\cos\chi\cdot\sigma_6),$$

$$\sigma_B=\sin^2\theta\left(\frac{1}{2}\sigma_1-\sigma_3\right)+(1+\cos^2\theta)(\cos 2\chi\cdot\sigma_2+\sin 2\chi\cdot\sigma_4)-\sin 2\theta(\sin\chi\cdot\sigma_5-\cos\chi\cdot\sigma_6),\tag{12}$$

$$\sigma_C=2\cos\theta(\sin 2\chi\cdot\sigma_2-\cos 2\chi\cdot\sigma_4)+2\sin\theta(\cos\chi\cdot\sigma_5-\sin\chi\cdot\sigma_6),$$

$$\sigma_D=\cos\theta\cdot\sigma_7+2\sin\theta(\cos\chi\cdot\sigma_8+\sin\chi\cdot\sigma_9),$$

where N_C is the color factor (in the case of the production of a lepton pair $N_C=1$, and in the case of the production of quarks $N_C=3$).

The correlation functions σ_a ($a=1\div 9$) in (12) depend on the scaling energies x_1 and x_2 ($x_H=2-x_1-x_2$) and they are easily determined on the basis of the fermionic tensor (6):

$$\sigma_1=\frac{x_H^2}{2x_{12}}(2-n_x^2),\quad \sigma_2=\frac{x_H^2}{4x_{12}}n_x^2,\qquad \sigma_3=\frac{x_H^2}{2x_{12}}(1-n_z^2),$$

$$\sigma_4=\frac{x_H^2}{2x_{12}}\cdot n_x n_z,\qquad \sigma_5=\sigma_6=\sigma_9=0.\quad \sigma_7=\frac{x_H^2}{x_{12}}\cdot n_z,\tag{13}$$

$$\sigma_8=\frac{x_H^2}{2x_{12}}\cdot n_x,$$

As can be seen, because of the orthogonality of the Y axis to the particle production plane, the correlation functions σ_5, σ_6 and σ_9 vanish. Under the condition $\dfrac{M_H^2}{s}\ll 1$ and $\dfrac{m_f^2}{s}\ll 1$ the distribution of particles in the Dalitz diagram is determined by the laws of conservation of energy and momentum:

$$x_1+x_2+x_H=2,\qquad x_1\vec{n}_1+x_2\vec{n}_2+x_H\vec{n}=0.$$

The boundaries of the allowed domain are determined by the equations $x_k=\left|x_i\pm x_j\right|$ $(i\neq j\neq k)$. Direct $x_1=x_2$, $x_1=x_H$ and $x_2=x_H$ divide the Dalitz diagram into six different regions. In the region (i; j) the scaling energies of the particles x_i and x_j satisfy the conditions

$$x_i\geq x_j\geq x_k\ (i\neq j\neq k).$$

We can direct the axis Z along the most energetic particle and select the axis X so that the x-projection of the momentum of the second more energetic particle becomes positive. Then the following areas of the Dalitz diagram are obtained.

Ia (3; 1). The axis Z is directed along the momentum of a more energetic Higgs boson, and the momentum of the second energetic fermion has a positive x-projection (see Fig. 2a)

$$\vec{n}=(0,\ 0,\ 1),\ \ \vec{n}_1=(s_{31},\ 0,\ c_{31}),\ \ \vec{n}_2=(-s_{32},\ 0,\ c_{32}).$$

Similarly we have the reduced regions:

Iб(3; 2): $\vec{n}=(0,\ 0,\ 1),\ \ \vec{n}_1=(-s_{31},\ 0,\ c_{31}),\ \ \vec{n}_2=(s_{32},\ 0,\ c_{32}).$

IIa(1; 3): $\vec{n}_1=(0,\ 0,\ 1),\ \ \vec{n}_2=(-s_{12},\ 0,\ c_{12}),\ \ \vec{n}=(s_{13},\ 0,\ c_{13});$

IIб(1; 2): $\vec{n}_1=(0,\ 0,\ 1),\ \ \vec{n}_2=(s_{12},\ 0,\ c_{12}),\ \ \vec{n}=(-s_{13},\ 0,\ c_{13});$

IIIa(2; 3): $\vec{n}_2=(0,\ 0,\ 1),\ \ \vec{n}_1=(-s_{21},\ 0,\ c_{21}),\ \ \vec{n}=(s_{23},\ 0,\ c_{23});$

IIIб(2; 1): $\vec{n}_2=(0,\ 0,\ 1),\ \ \vec{n}_1=(s_{21},\ 0,\ c_{21}),\ \ \vec{n}=(-s_{23},\ 0,\ c_{23}).$

Here we have introduced the notation $s_{ij} = \sin\theta_{ij}$ and $c_{ij} = \cos\theta_{ij}$, where θ_{ij} − the angle between the directions of the particle momenta i and j. These angles depend on the scaling energies of the particles

$$\sin\theta_{ij} = \frac{2\sqrt{(1-x_1)(1-x_2)(1-x_H)}}{x_i x_j}, \qquad \cos\theta_{ij} = 1 - \frac{2(x_i + x_j - 1)}{x_i x_j}. \tag{14}$$

Using these relations, we can easily determine the correlation functions in each region of the Dalitz diagram. Here we give the correlation functions in the coordinate system Ia (Ib), where the momentum of the more energetic Higgs boson is directed along the axis Z, and the second energetic fermion (antifermion) in the production plane has a positive momentum projection $q_{1x} > 0$ ($q_{2x} > 0$):

$$\sigma_1 = \sigma_7 = \frac{x_H^2}{(1-x_1)(1-x_2)} = 2 + \frac{1-x_1}{1-x_2} + \frac{1-x_2}{1-x_1}, \qquad \sigma_2 = \sigma_3 = \sigma_4 = \sigma_8 = 0. \tag{15}$$
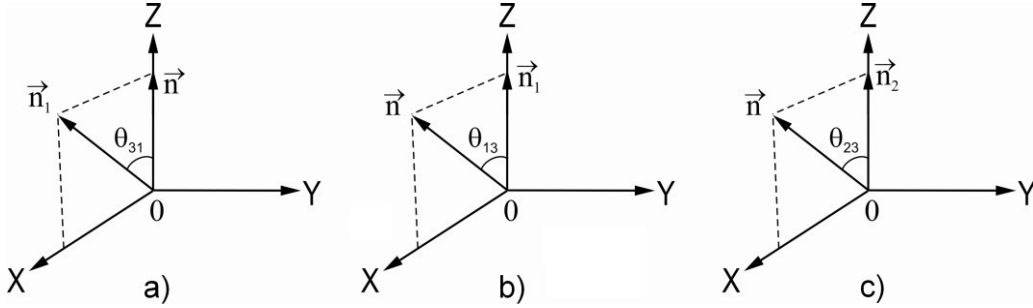

Fig. 2. Coordinate systems Ia, IIa and IIIa

Integrating the cross section (11) along the azimuthal angle φ, we obtain the particle distribution over the angles θ and χ in the case of longitudinally polarized $e^- e^+$ - and $f\bar{f}$ -pars

$$\frac{d^4\sigma}{d\chi d(\cos\theta)dx_1 dx_2} = \frac{\alpha_{KED}^2 Q_f^2 N_C}{256\pi^2 s} g_{H_{SM}ff}^2 (\sigma_1 + 2\sigma_3)\{(1 + h_1 h_2)(1 - \lambda_1\lambda_2)[1 + \alpha_1 \cos^2\theta +$$

$$+ \alpha_2 \sin^2\theta\cos 2\chi + \alpha_4 \sin^2\theta\sin 2\chi] + (h_1 + h_2)(\lambda_2 - \lambda_1)[\alpha_7 \cos\theta + \alpha_8 \sin\theta\cos\chi]\}, \tag{16}$$

where the coefficients of the angular distributions of particles:

$$\alpha_1 = \frac{\sigma_1 - 2\sigma_3}{\sigma_1 + 2\sigma_3}, \quad \alpha_2 = \frac{2\sigma_2}{\sigma_1 + 2\sigma_3}, \quad \alpha_4 = \frac{2\sigma_4}{\sigma_1 + 2\sigma_3}, \quad \alpha_7 = \frac{2\sigma_7}{\sigma_1 + 2\sigma_3}, \quad \alpha_8 = \frac{4\sigma_8}{\sigma_1 + 2\sigma_3}. \tag{17}$$

It follows from the formula of the differential cross section (16) that the electron and the positron must have opposite helicities $\lambda_1 = -\lambda_2 = \pm 1$ (the electron is left, and the positron is right − $e_L^- e_R^+$, or the electron is right, and the positron is left − $e_R^- e_L^+$), while the helicities of the fermion and antifermion must be the same − $h_1 = h_2 = \pm 1$ (fermion and antifermion right − $f_R \bar{f}_R$ or left − $f_L \bar{f}_L$). Thus, four spiral sections correspond to the process $e^- + e^+ \to H_{SM} + f + \bar{f}$:

1) electron, fermion and antifermion are left polarized, and positron is right:

$$\frac{d^4\sigma(e_L^- e_R^+ \to H_{SM} f_L \bar{f}_L)}{d\chi d(\cos\theta)dx_1 dx_2} = \frac{\alpha_{KED}^2 Q_f^2 N_C}{64\pi^2 s} g_{H_{SM}ff}^2 (\sigma_1 + 2\sigma_3)[1 + \alpha_1 \cos^2\theta +$$

$$+ \alpha_2 \sin^2\theta\cos 2\chi + \alpha_4 \sin^2\theta\sin 2\chi - \alpha_7 \cos\theta - \alpha_8 \sin\theta\cos\chi];$$

2) the electron, fermion and antifermion are right polarized, and the positron is left:

$$\frac{d^4\sigma(e_R^- e_L^+ \to H_{SM} f_R \bar{f}_R)}{d\chi d(\cos\theta) dx_1 dx_2} = \frac{\alpha_{KED}^2 Q_f^2 N_C}{64\pi^2 s} g_{H_{SM}ff}^2 (\sigma_1 + 2\sigma_3)[1 + \alpha_1 \cos^2\theta +$$

$$+ \alpha_2 \sin^2\theta \cos 2\chi + \alpha_4 \sin^2\theta \sin 2\chi - \alpha_7 \cos\theta - \alpha_8 \sin\theta \cos\chi];$$

3) the electron is polarized to the left, and the positron, fermion, and antifermion are right:

$$\frac{d^4\sigma(e_L^- e_R^+ \to H_{SM} f_R \bar{f}_R)}{d\chi d(\cos\theta) dx_1 dx_2} = \frac{\alpha_{KED}^2 Q_f^2 N_C}{64\pi^2 s} g_{H_{SM}ff}^2 (\sigma_1 + 2\sigma_3)[1 + \alpha_1 \cos^2\theta +$$

$$+ \alpha_2 \sin^2\theta \cos 2\chi + \alpha_4 \sin^2\theta \sin 2\chi + \alpha_7 \cos\theta + \alpha_8 \sin\theta \cos\chi];$$

4) the electron is polarized right, and the positron, fermion and antifermion are left:

$$\frac{d^4\sigma(e_R^- e_L^+ \to H_{SM} f_L \bar{f}_L)}{d\chi d(\cos\theta) dx_1 dx_2} = \frac{\alpha_{KED}^2 Q_f^2 N_C}{64\pi^2 s} g_{H_{SM}ff}^2 (\sigma_1 + 2\sigma_3)[1 + \alpha_1 \cos^2\theta +$$

$$+ \alpha_2 \sin^2\theta \cos 2\chi + \alpha_4 \sin^2\theta \sin 2\chi + \alpha_7 \cos\theta + \alpha_8 \sin\theta \cos\chi].$$

It is of interest to compare the cross sections of processes $e^- + e^+ \to q + \bar{q} + g$ and $e^- + e^+ \to q + \bar{q} + H_{SM}$ in the case of longitudinally polarized particles, where $g-$ the gluon emitted by the quark and antiquark. Calculations show that in the process $e^- + e^+ \to q + \bar{q} + g$ the quark and antiquark must possess opposite helicities ($q_L \bar{q}_R$ or $q_R \bar{q}_L$) [16]. In the process $e^- + e^+ \to q + \bar{q} + H_{SM}$ considered here, the quark and antiquark should be polarized either left ($q_L \bar{q}_L$) or right ($q_R \bar{q}_R$)

We estimate the coefficients of the angular distributions α_i ($i = 1, 2, 4, 7, 8$) in the coordinate system IIIa, where the momentum of the antifermion is oriented along the Z axis, and the momentum of Higgs boson in the production plane has a positive x-projection (Fig. 2c). Using the expressions for the correlation functions given in the Appendix, for these coefficients we have the expressions:

$$\alpha_1 = \frac{3c_{23}^2 - 1}{3 - c_{23}^2}, \quad \alpha_2 = \frac{s_{23}^2}{3 - c_{23}^2}, \quad \alpha_4 = -\frac{2s_{23}c_{23}}{3 - c_{23}^2}, \quad \alpha_7 = \frac{4c_{23}}{3 - c_{23}^2}, \quad \alpha_8 = -\frac{4s_{23}}{3 - c_{23}^2}.$$
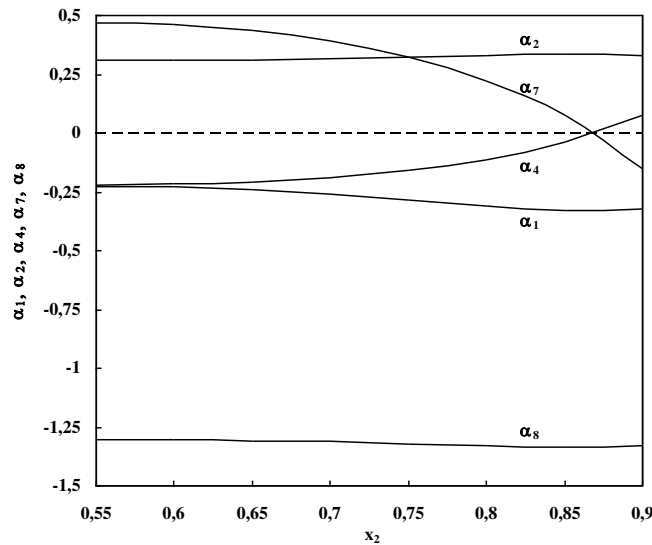

Fig.3. Dependence of the angular distribution coefficients on x_2 at $x_1 = 0,9$ in the reaction $e^- e^+ \to H_{SM} \tau^- \tau^+$.

Fig. 3 shows the dependence of the angular distribution coefficients on the scaling energy x_2 for a fixed $x_1 = 0,9$ in process $e^- + e^+ \rightarrow H_{SM} + \tau^- + \tau^+$. As can be seen, the coefficients α_1 and α_8 are negative and decrease x_2 slowly with increasing. The coefficient α_2 is positive and increases x_2 slowly with increasing. As for the coefficients α_4 and α_7, we note that at the beginning of the spectrum the coefficient α_4 (α_7) is negative (positive) and with increasing x_2 it monotonically increases (decreases) and vanishes, and then becomes positive (negative).

Summing (averaging) the differential cross section (16) over the polarization states of the anti- fermion (positron) and integrating with respect to the angle χ, we have

$$\frac{d^3\sigma}{d(\cos\theta)dx_1 dx_2} = \frac{\alpha_{KED}^2 Q_f^2 \, Nc}{128\pi s} g_{H_{SM}ff}^2 (\sigma_1 + 2\sigma_3) \times$$
$$\times [1 + \alpha_1(x_1, x_2)\cos^2\theta - h_1\lambda_1\alpha_7(x_1, \, x_2)\cos\theta]. \tag{18}$$

It follows that if the electron is longitudinally polarized, then in the process $e^- + e^+ \rightarrow H_{SM} + f + \bar{f}$ the fermion can acquire longitudinal polarization. The degree of longitudinal polarization of the fermion is determined in the standard manner

$$P_f(x_1, x_2, \cos\theta) = -\lambda_1 \cdot \frac{\alpha_7(x_1, x_2)\cos\theta}{1 + \alpha_1(x_1, x_2)\cos^2\theta}. \tag{19}$$

The degree of longitudinal polarization (19) can be conveniently investigated in the process $e^- + e^+ \rightarrow H_{SM} + \tau^- + \tau^+$, since by investigating the decay channels in $\tau^- \rightarrow \pi^- + \nu_\tau$, $\tau^- \rightarrow K^- + \nu_\tau$ experiments it is possible to determine the degree of longitudinal polarization of the τ^--lepton.

Fig. 4 illustrates the angular dependence of the degree of longitudinal polarization of a τ^--lepton for $\lambda_1 = -1$ a fixed $x_1 = 0,9$, $x_2 = 0,6$ and $x_1 = 0,9$, $x_2 = 0,8$. As can be seen, with increasing angle θ, the degree of longitudinal polarization decreases and reaches a minimum at the end of the angular spectrum. The growth of the scaling energy x_2 leads to a decrease in the degree of longitudinal polarization of the τ^--lepton.
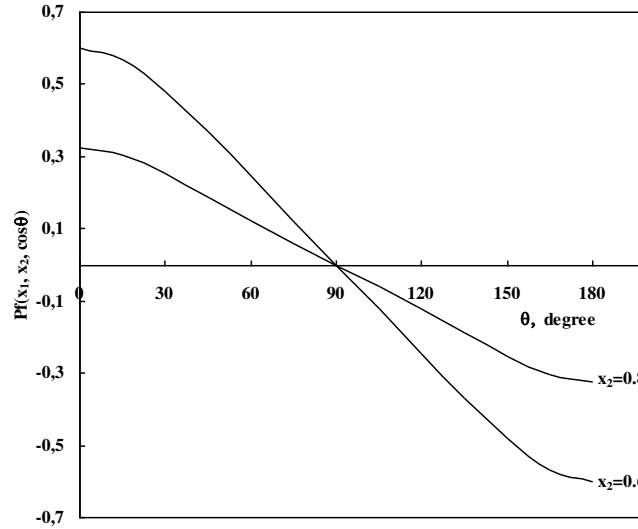

Fig. 4. Angular dependence of the degree of longitudinal polarization of τ^--lepton

Fig. 5 shows the dependence of the degree of longitudinal polarization of τ^--lepton on the change x_2 for a fixed energy $x_1 = 0,9$ and for different angles θ of emission of particles. When the degree $0 \leq \theta < 90°$ of longitudinal polarization it is positive, and for $90° < \theta \leq 180°$ it is negative.

Now consider the particle distribution over the angles θ and φ. To do this, we integrate the cross section (11) along the azimuthal angle χ of the ($e^- e^+$-pair is polarized transversely):

$$\frac{d^4\sigma}{d\varphi d(\cos\theta)dx_1 dx_2} = \frac{\alpha_{KED}^2 Q_f^2 N_C}{128\pi^2 s} g_{H_{SM}ff}^2 (\sigma_1 + 2\sigma_3)(1+\alpha_1 \cos^2\theta)\times$$

$$\times [1 + A_\perp(x_1, x_2, \cos\theta)\eta_1\eta_2 \cos 2\varphi]. \qquad (20)$$

Here $A_\perp(x_1, x_2, \cos\theta)$ is the transverse spin asymmetry due to the transverse polarizations of the $e^- e^+$-pair and determined by the relation

$$A_\perp(x_1, x_2, \cos\theta) = \frac{\alpha_1(x_1, x_2)\sin^2\theta}{1+\alpha_1(x_1, x_2)\cos^2\theta}. \qquad (21)$$
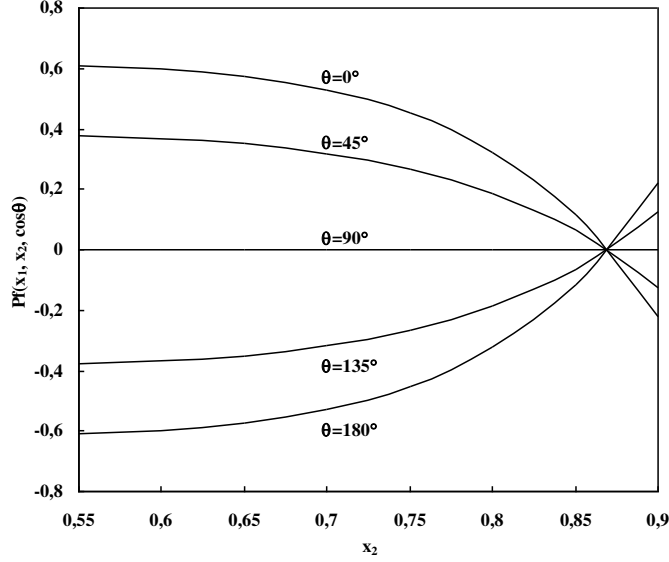

Fig. 5. The dependence of the degree of longitudinal polarization of a τ^--lepton on the change x_2 at a fixed energy $x_1 = 0,9$ and different angles θ of emission of particles.

Fig. 6 illustrates the angular dependence of the transverse spin asymmetry in the process $e^- + e^+ \rightarrow H_{SM} + \tau^- + \tau^+$ for a fixed x_1 =0,95, x_2 =0,55 and x_2 =0,65. As the angle θ increases, the degree of transverse spin asymmetry increases and reaches a maximum at $\theta = 90°$, and a further increase of the angle leads to a decrease in the asymmetry. With increasing scaling energy x_2, the transverse spin asymmetry decreases.
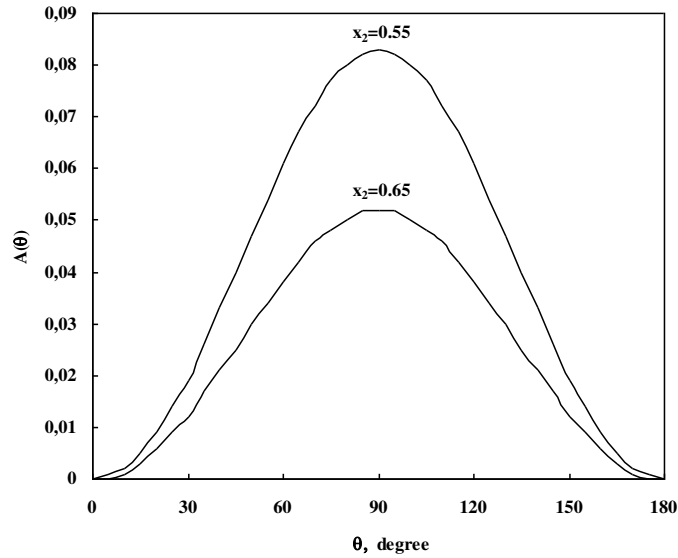

Fig. 6. Angular dependence of the transverse spin asymmetry in the process $e^- e^+ \rightarrow H_{SM}\tau^- \tau^+$.

Integrating the cross section (20) over the angles θ and φ, we obtain the energy spectrum of the particles, which

coincides with the result of [17]

$$\frac{d^2\sigma}{dx_1 dx_2} = \frac{\alpha^2_{KED} Q_f^2 N_C}{12\pi s} g^2_{H_{SM} ff} \cdot \left(2 + \frac{1-x_1}{1-x_2} + \frac{1-x_2}{1-x_1}\right).$$ (22)

Fig. shows the dependence of the differential cross section (22) on the variable x_2 for fixed $x_1 = 0{,}9$ and $0{,}95$. As the variable x_2 increases, the differential cross section decreases monotonically, and the growth of the τ^--lepton energy x_1 leads to an increase in the cross section.
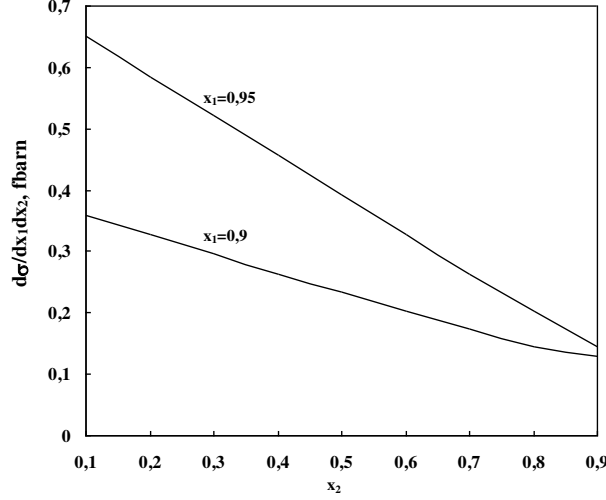

Fig. 7. The dependence of the differential cross section of the process $e^- e^+ \to H_{SM} \tau^- \tau^+$ from a variable x_2 for a fixed $x_1 = 0{,}9$ and $0{,}95$

We introduce new variables $T = T_1 = \max(x_1, x_2, x_H)$, T_2 and T_3 so that the inequalities $T = T_1 \geq T_2 \geq T_3 = 2 - T - T_2$ are satisfied. We select the axis Z along the momentum of the most energetic particle and carry out integration over the variable T_2 for a fixed T one. As a result, we find the cross section $\frac{d\sigma}{dT}$ of the process $e^- + e^+ \to H_{SM} + f + \bar{f}$ as a function T. For $x_H = T$ and $x_1 = T_2$ and (or $x_2 = T_2$) the cross section is:

$$\frac{d\sigma}{dT} = \frac{\alpha^2_{KED} Q_f^2 N_C}{12\pi s} g^2_{H_{SM} ff} \cdot T \ln\left(\frac{1-T}{T}\right).$$ (23)

For $x_1 = T$ and $x_H = T_2$ (or for $x_2 = T$ and $x_H = T_2$) we have a section:

$$\frac{d\sigma}{dT} = \frac{\alpha^2_{KED} Q_f^2 N_C}{12\pi s} g^2_{H_{SM} ff} \cdot \left[\frac{(3T-2)(6-5T)}{2(1-T)} - (1-T)\ln\left(\frac{2T-1}{1-T}\right)\right].$$ (24)

If, however, $x_1 = T$ and $x_2 = T_2$ (or if $x_2 = T$ and $x_1 = T_2$), then the cross section

$$\frac{d\sigma}{dT} = \frac{\alpha^2_{KED} Q_f^2 N_C}{12\pi s} g^2_{H_{SM} ff} \cdot \left[\frac{(3T-2)(2-T)}{2(1-T)} + (1-T)\ln\left(\frac{2T-1}{T}\right)\right].$$ (25)

Adding the expressions (23)-(25), we obtain a section characterizing the distribution of the most energetic particle with respect to the variable T:

$$\frac{d\sigma}{dT} = \frac{\alpha^2_{KED} Q_f^2 N_C}{12\pi s} g^2_{H_{SM} ff} \cdot \left[\frac{(3T-2)(4-3T)}{1-T} + \ln\left(\frac{2T-1}{T}\right)\right].$$ (26)

Fig. 8 shows the dependence of the reaction $e^- + e^+ \to H_{SM} + \tau^- + \tau^+$ cross section on the variable T for $\sqrt{s} = 1$ TeV and $m_\tau = 1{,}778$ GeV. An increase in the variable T from $0{,}725$ to $0{,}9$ leads to a monotonic increase in the cross section of the reaction from $0{,}012$ fbarn to $0{,}448$ fbarn.
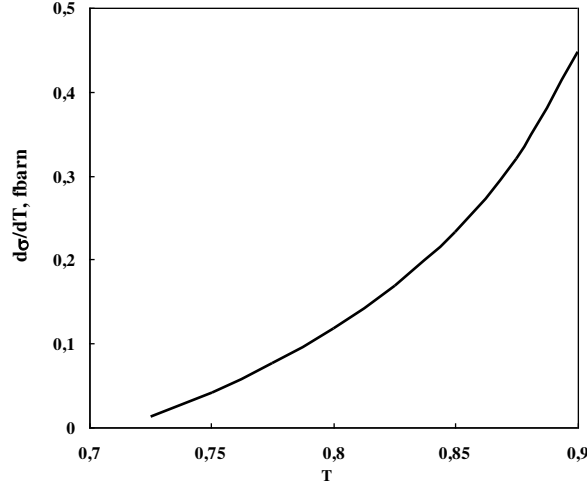
Fig. 8. The dependence of the cross section of the process $e^-e^+ \rightarrow H_{SM}\tau^-\tau^+$ on the variable T.

4. The production of the Higgs bosons of the MSSM and the fermion pair

Along with SM, the Minimal Supersymmetric Standard Model (MSSM) [7, 18] is widely discussed in the literature, where two doublets of a complex scalar field with hypercharges -1 and +1 are introduced:

$$\varphi_1 = \begin{pmatrix} H_1^0 \\ H_1^- \end{pmatrix}, \qquad \varphi_2 = \begin{pmatrix} H_2^+ \\ H_2^0 \end{pmatrix}.$$

After the spontaneous breaking of the MSSM, five Higgs particles appear: CP-even h- and H-bosons, CP-odd A-boson and charged H^+- and H^--bosons. In high-energy electron-positron collisions, in addition to the process $e^- + e^+ \rightarrow H_{SM} + f + \bar{f}$, there can also occur reactions of the production of Higgs bosons MSSM and the fermion pair: $e^- + e^+ \rightarrow H + f + \bar{f}$, $e^- + e^+ \rightarrow h + f + \bar{f}$ and $e^- + e^+ \rightarrow A + f + \bar{f}$. According to the MSSM, the interaction constants of these bosons with the fermion pair are determined by the expressions [18]:

$$g_{Hff} = \frac{m_f}{\eta} \cdot \frac{\sin\alpha}{\sin\beta}, \quad g_{hff} = \frac{m_f}{\eta} \cdot \frac{\cos\alpha}{\sin\beta}, \quad g_{Aff} = \frac{m_f}{\eta} \cdot tg\beta,$$

where α and β are the MSSM parameters. Consequently, the differential cross sections of the processes $e^- + e^+ \rightarrow H + f + \bar{f}$ and $e^- + e^+ \rightarrow h + f + \bar{f}$ will differ from the reaction $e^- + e^+ \rightarrow H_{SM} + f + \bar{f}$ cross section by the presence of an additional factor $\dfrac{\sin\alpha}{\sin\beta}$ and $\dfrac{\cos\alpha}{\sin\beta}$. As for the process $e^- + e^+ \rightarrow A + f + \bar{f}$, we note that, because of the pseudoscalarity of the A-boson, the expression for the fermion current (3) is replaced by the current:

$$J_\mu = \bar{u}_f(q_1) \left[\gamma_5 \frac{\hat{q}_1 + \hat{k} + m_f}{(q_1 + k)^2 - m_f^2} \gamma_\mu - \gamma_\mu \frac{\hat{q}_2 + \hat{k} - m_f}{(q_2 + k)^2 - m_f^2} \gamma_5 \right] \upsilon_f(q_2).$$

Note that this current also leads to the results obtained earlier for the reaction $e^- + e^+ \rightarrow H_{SM} + f + \bar{f}$. Here, too, it is necessary to replace the interaction constant $g_{H_{SM}ff}$ by the constant g_{Aff}.

CONCLUSION

We discussed the processes production of a Higgs boson H_{SM} (boson MSSM H, h, A) and a heavy fermion e^-e^+-pair in annihilation of an arbitrarily polarized pair: $e^- + e^+ \rightarrow H_{SM} + f + \bar{f}$, $e^- + e^+ \rightarrow H + f + \bar{f}$, $e^- + e^+ \rightarrow h + f + \bar{f}$, $e^- + e^+ \rightarrow A + f + \bar{f}$. Analytical expressions are obtained for differential cross sections, angular and spin correlations. The features of the behavior of the cross sections, angular and spin correlations are investigated as a function of the energies and emission angles of the particles. The results are illustrated by graphs.

APPENDIX

Here we give the expressions for the correlation functions in coordinate systems IIa,b and IIIa, b
1) In systems IIa and IIb:

$$\sigma_1 = \frac{x_H^2}{2x_{12}}(2 - s_{13}^2), \quad \sigma_2 = \frac{x_H^2}{4x_{12}} \cdot s_{13}^2,$$

$$\sigma_3 = \frac{x_H^2}{2x_{12}}(1 - c_{13}^2), \quad \sigma_4 = \pm \frac{x_H^2}{2x_{12}} \cdot s_{13}c_{13},$$

$$\sigma_7 = \frac{x_H^2}{4x_{12}} \cdot c_{13}, \quad \sigma_8 = \pm \frac{x_H^2}{2x_{12}} \cdot s_{13};$$

2) In systems IIIa and IIIb:

$$\sigma_1 = \frac{x_H^2}{2x_{12}} \cdot (2 - s_{23}^2), \quad \sigma_2 = \frac{x_H^2}{2x_{12}} \cdot \frac{1}{2}s_{23}^2,$$

$$\sigma_3 = \frac{x_H^2}{2x_{12}} \cdot (1 - c_{23}^2), \quad \sigma_4 = \pm \frac{x_H^2}{2x_{12}} \cdot s_{23}c_{23},$$

$$\sigma_7 = \frac{x_H^2}{2x_{12}} \cdot 2c_{23}, \quad \sigma_8 = \pm \frac{x_H^2}{2x_{12}} \cdot c_{23}.$$

The upper sign corresponds to systems IIa and IIIa, and the lower sign corresponds to IIb and IIIb.

———————————————

[1] *S.K. Abdullayev.* Standart model, lepton və kvarkların xassələri. Bakı, «Zəka print», 2017, 274s.
[2] *A. Djouadi.* The Anatomy of Electro-Weak Symmetry Breaking. Tome I: The Higgs boson in the Standard Model. arXiv: hep-ph/0503172v2, 2005; DOI: 10.1016/j.physrep.2007.10.004
[3] ATLAS Collaboration. Observation of a new particle in the search for the Standard Model Higgs boson with the ATLAS detector at the LHC // Phys. Letters, 2012, B 716, p. 1-29
[4] CMS Collaboration. Observation of a new boson at mass of 125 *GeV* with the CMS experiment at the LHC // Phys. Letters, B 716, p. 30-61.
[5] *P.W. Higgs.* Broken Symmetries and the masses of gauge bosons // Phys. Rev. Lett., 1964, V. 13, p.508.
[6] *C.A. Lester.* Search for the Higgs boson produced in association with top quarks in multilepton final states at ATLAS, University of Pensilvania, ScholarlyCommons.
http://repositoryenn.edn/edissertations, 2015.
[7] *R.R. Barman et al.* Current status of MSSM Higgs sector with LHC 13 TeV data // arXiv: 1608.02573v3 [hep-ph]. 2017 23 may.
[8] *S.K. Abdullayev, M.Sh. Gojayev, F.A. Saddigh.* Decay Channels of the Standard Higgs Boson // Moscow University Physics Bulletin, 2017, Vol.72, №4, pp.329-339; published in Vestnik Moscovskoqo Universiteta, Seriya 3: Physics, Astronomy, 2017, №4, s.3-11.
[9] *S.K. Abdullayev, M.Sh. Gojayev, N.E. Nesibova.* Production of scalar boson and neutrino pair in longitudinally polarized electron-positron colliding beams // Azerbaijan Journal of Physics: Fizika, 2017, XXIII, N. 3, p. 45-52.
[10] *S.K. Abdullayev, M.Sh. Gojayev, N.E. Nesibova.* Rojdeniye skalyarnoqo bozona i fermionnoy parı na proizvolno polyarizovannix e⁻e⁺-puchkax // İzvestiya VUZov, Fizika, 2018, t. , s. (in Russian).
[11] *S.K. Abdullayev, M.Sh. Gojayev.* The Higgs bosons production in arbitrary polarized electron-positron colliding beams // UZFF Moskovskoqo Universiteta, 2018. N. 1. s.1810101-1 (in Russian).
[12] *S.K. Abdullayev, M.Sh. Gojayev, N.E. Nesibova, G.A. Soltanova.* The production of the higgs boson and $t\bar{t}$-pair in polarized e⁻e⁺-beams // Azerbaijan Journal of Physics: Fizika, 2018, **XXIV**, N. 1, p. 33-40.
[13] *V.D. Shiltsev.* High-energy particle colliders: past 20 years, next 20 years, and beyond // Physics-Uspekhi, 2012, Vol. 55, N. 10, p.965-976.
[14] *K. Peters.* Prospects for beyond Standard Model Higgs boson searches at future LHC runs and other machines // arXiv: 1701.05124v2 [hep-ex]. 2017
[15] Gunion J.F. Muon Colliders: The Machine and The Physics. Preprint UCD-97-17, Julay 1997, University of California-Davis.
[16] *S.K. Abdullayev.* Effects of the superstring Z' boson in the reactions $e^-e^+ \to q\bar{q}g$ and $e^-e^+ \to \tilde{q}\tilde{\bar{q}}g$ // Physics of Atomic Nuclei, 1997, V. 60, N. 11, p. 1901-1919.
[17] *K.J.F. Gaemers, G.J. Gounaris.* Bremsstrahlung Production of Higgs boson in e⁻e⁺-collisions // Phys. Lett., 1978, V. 77B, N. 4-5, p. 379-382.
[18] *A. Djouadi.* The Anatomy of Electro-Weak Symmetry Breaking. Tome II: The Higgs in Minimal Supersymmetric Model. arXiv: hep-ph/0503173v2, 2003;

DECAYS OF SUPERSYMMETRIC HIGGS BOSONS INTO FERMIONS

S.K. ABDULLAYEV, E.Sh. OMAROVA

[1] *Baku State University, Azerbaijan, AZ 1148, Baku, Z. Khalilova str., 23,*
[a]*sabdullayev@bsu.edu.az,* [b]*emiliya.abdullayeva@inbox.ru*

In the framework of the Minimal Supersymmetric Standard Model we investigated the decay channels of Higgs bosons $H(h, A), H^\pm$ into arbitrarily polarized fermions: $H(h, A) \to f\bar{f}$, $H^+ \to f\bar{f}'$, $H(A) \to f\bar{f}'W^-$, $H^+ \to f\bar{f}W^+$. Analytical expressions for the widths of these decays are obtained, the transverse spin asymmetries and the degree of longitudinal polarization of fermion are determined. The dependence of the asymmetries and the widths of the decays on the mass of the Higgs bosons are studied.

Keywords: Minimal Supersymmetric Standard Model, Higgs boson, fermion pair, decay width, helicity.
PACS: 12.15-y, 12.15 Mm, 14.70 Hp, 14.80 Bn.

1. INTRODUCTION

Standard model (SM) interactions of elementary particles is a combination theory of electroweak interactions based on the symmetry group $SU_L(2) \times U_Y(1)$ and Quantum Chromodynamics (QCD), based on a gauge group $SU_C(3)$. The Group $SU_L(2) \times U_Y(1)$ has satisfactorily describes electroweak interactions leptons, quarks and gauge bosons [1-3] and QCD-strong interactions of quarks and gluons [4, 5].

The amazing feature of CM is the phenomenon of spontaneous electroweak symmetry group violations as a result of which gauge bosons, the charged leptons and quarks are acquire mass [1-3]. A doublet of scalar fields $\varphi = \begin{pmatrix} \varphi^+ \\ \varphi^0 \end{pmatrix}$ is introduced into the theory, the neutral component of which has a vacuum value different from zero. As a result of the electroweak group $SU_L(2) \times U_Y(1)$ spontaneously broken to electromagnetic symmetry group $U_Q(1)$. Three of the four components of a scalar field φ absorbed $W^\pm$ - и Z^0 -vector bosons. The fourth component neutral condition of the scalar field is the Higgs boson H_{SM}.

In various laboratories in the world carried out searches for Higgs bosons. Discover the Higgs boson H_{SM} and study its physical properties was one of the main tasks of the large Hadron Collider (LHC). Finally, in 2012 year a scalar Higgs boson has been discovered at the LHC collider by the ATLAS and CMS collaborations [6.7] (see also reviews [8-10]), and this began a new phase of research to determine the nature of this particle.

It should be noted that along with SM, widely discussed in the literature the Minimal Supersymmetric Standard Model (MSSM) [11-13]. Here, in contrast to SM injected two doublet complex scalar field with hyper-charges-1 and 1

$$\varphi_1 = \begin{pmatrix} H_1^0 \\ H_1^- \end{pmatrix}, \quad \varphi_2 = \begin{pmatrix} H_2^+ \\ H_2^0 \end{pmatrix}.$$

To obtain the physical fields of the Higgs bosons, the fields φ_1 and φ_2 are represented in the form

$$\varphi_1 = \frac{1}{\sqrt{2}} \begin{pmatrix} \upsilon_1 + H_1^0 + iP_1^0 \\ H_1^- \end{pmatrix},$$

$$\varphi_2 = \frac{1}{\sqrt{2}} \begin{pmatrix} H_2^+ \\ \upsilon_2 + H_2^0 + iP_2^0 \end{pmatrix}.$$

Here $H_1^0, P_1^0, H_2^0, P_2^0$ are fields that describe the excitation system on vacuum states $\langle \varphi_1 \rangle = \frac{1}{\sqrt{2}} \upsilon_1$ and $\langle \varphi_2 \rangle = \frac{1}{\sqrt{2}} \upsilon_2$.

Mixing fields H_1^0 and H_2^0, get CP-even Higgs bosons H and h (mixing angle α):

$$\begin{pmatrix} H \\ h \end{pmatrix} = \begin{pmatrix} \cos\alpha & \sin\alpha \\ -\sin\alpha & \cos\alpha \end{pmatrix} \begin{pmatrix} H_1^0 \\ H_2^0 \end{pmatrix}.$$

Similarly, mixing the fields P_1^0 and P_2^0, and also $H_1^\pm$ and $H_2^\pm$, we obtain a CP-odd Higgs boson A and charged Higgs bosons H^+ and H^- (mixing angle β):

$$\begin{pmatrix} G^0 \\ A \end{pmatrix} = \begin{pmatrix} \cos\beta & \sin\beta \\ -\sin\beta & \cos\beta \end{pmatrix} \begin{pmatrix} P_1^0 \\ P_2^0 \end{pmatrix},$$

$$\begin{pmatrix} G^\pm \\ H^\pm \end{pmatrix} = \begin{pmatrix} \cos\beta & \sin\beta \\ -\sin\beta & \cos\beta \end{pmatrix} \begin{pmatrix} H_1^\pm \\ H_2^\pm \end{pmatrix}.$$

G^0 And $G^\pm$ − neutral and charged Goldstone bosons.

Consequently, after the spontaneous symmetry breaking, five Higgs particles appear in the MSSM: CP-even h - and H -bosons, CP-odd A -bison and charged H^+ - and H^- -bosons.

In the MSSM, the Higgs sector is characterized by six parameters $M_h, M_H, M_A, M_{H^\pm}, \alpha$ and β. Of these,

only two parameters are free, such parameters usually take the mass M_A and the parameter $tg\beta$. This parameter is equal to the ratio $\dfrac{\upsilon_2}{\upsilon_1}$ and varies within

$$1 \leq \tan\beta \leq \frac{m_t}{m_b} = 35.5,$$

where $m_t = 173.2$ GeV and $m_b = 4.88$ GeV are the masses of t - and b -quarks.

The masses of CP- odd h - and H -bosons (charged $H^{\pm}$ -bosons) are expressed by the masses M_A and M_Z (M_A and M_W):

$$M_{h(H)}^2 = \frac{1}{2}[M_A^2 + M_Z^2 \mp \sqrt{\left(M_A^2 + M_Z^2\right)^2 - 4M_A^2 M_Z^2 \cos^2 2\beta}], \quad M_{H^{\pm}}^2 = M_A^2 + M_W^2.$$

Figure 1 shows the dependence of the masses h -, H - and H^+ -bosons as a function of the mass of the pseudoscalar A -boson at a value of the parameter $tg\beta = 3$ and masses $M_Z = 91.1875$ GeV, $M_W = 80.385$ GeV. With an increase the mass of the A -boson from 100 GeV to 400 GeV, the mass of the light h -boson varies from 60 GeV to 72.255 GeV while the masses of the $H(H^+)$ -bosons vary from 121.216 (128.303) GeV up to 403.85 (407.987) GeV.
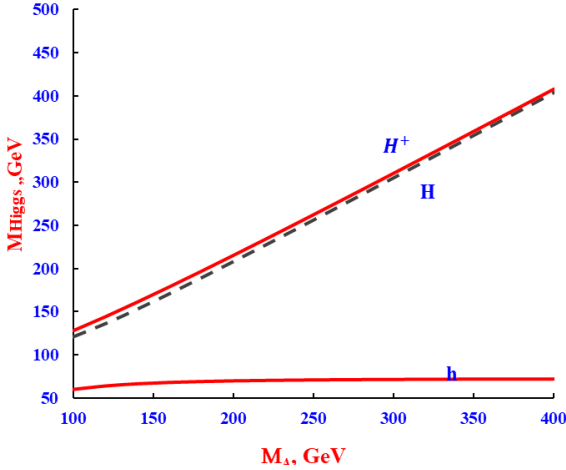
$$H^+ \to f + \overline{f'}, \qquad (2)$$

$$H(A) \to t + \overline{b} + W^-, \qquad (3)$$

$$H^{\pm} \to b + \overline{b} + W^{\pm}, \qquad (4)$$

Here $f\overline{f}$ ($f\overline{f'}$) is a fermion (lepton or quark) pair. These channels of Higgs bosons decay were previously considered in a number of papers (see [11] and there references to primary sources). However, in these papers the polarization states of fermions are not considered. Our analysis shows that the study of the polarization characteristics of fermions in these decays can provide valuable information on the nature of Higgs bosons. We obtained analytical expressions for the width of the reduced decays with allowance for arbitrary polarization of the fermions, the dependence of the decay width and spin asymmetries on the mass of the Higgs bosons was studied.

Fig.1. The dependence of the masses of the h -, H - and H^+ - bosons on the mass M_A

The mixing angles of the fields α and β are related by:

$$\tan 2\alpha = \tan 2\beta \frac{M_A^2 + M_Z^2}{M_A^2 - M_Z^2}, \quad \left(-\frac{\pi}{2} \leq \alpha < 0\right).$$

We note that the decay channels of the standard Higgs boson have been studied in a number of works [2, 14-18]. In this paper we have studied the decays of the Higgs bosons of MSSM through channels:

$$h(H; A) \to f + \overline{f}, \qquad (1)$$

2. THE DECAYS OF $h(H; A) \to f + \overline{f}$

The Feynman diagram of the decay of a neutral Higgs boson into a fermion pair is shown in Fig. 2, where four impulses and the polarization vectors of the particles are written in parentheses.
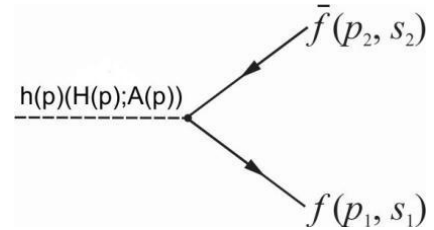

Fig.2. The Feynman diagram of the decay $h(H; A) \to f + \overline{f}$

MSSM claims that the h - and H -bosons are CP - even particles, and the A -boson CP is odd. In this connection, we consider the decay of a boson Φ whose interaction with the fermion pair simultaneously contains the CP - even and odd components:

$$M(\Phi \to f\overline{f}) = g_{\Phi ff}[\overline{u}_f(p_1, s_1)(a + b\gamma_5)\upsilon_f(p_2, s_2)]\Phi(p), \qquad (5)$$

where $g_{\Phi ff}$ is the interaction constant of the Φ-boson with the fermion pair, a and b are some constant parameters,, and for $a = 1$ and $b = 0$ we obtain the decay amplitudes of the CP-even h- and H-bosons, and for $a = 0$ and $b = 1$ it is the decay amplitude of the

pseudoscalar A-boson, $\Phi(p)$ is the wave function of the Φ boson normalized to unity.

The width of the decay of the Φ boson into a fermion pair is proportional to the square of the matrix element (5):

$$\frac{d\Gamma(\vec{\xi}_1, \vec{\xi}_2)}{d\Omega} = \frac{\beta_f}{64\pi^2 M_\Phi}\left|M(\Phi \to f\bar{f})\right|^2 = \frac{N_C \beta_f}{128\pi^2} g_{\Phi ff}^2 M_\Phi \qquad \{|a|^2 \beta_f^2 [1 + (\vec{\xi}_1 \vec{\xi}_2) - 2(\vec{n}\vec{\xi}_1)(\vec{n}\vec{\xi}_2)] + |b|^2 [1 - (\vec{\xi}_1\vec{\xi}_2)] +$$

$$+ 2\,\mathrm{Re}(ab^*)\beta_f[(\vec{n}\vec{\xi}_1) - (\vec{n}\vec{\xi}_2)] + 2\,\mathrm{Im}(ab^*)\beta_f\,(\vec{n}[\vec{\xi}_1\vec{\xi}_2])\}, \qquad (6)$$

where N_C is the color factor ($N_C = 1$ for the production of the lepton pair and $N_C = 3$ for the production of the quark pair), m_f and M_Φ are the fermion and Φ boson masses, $\beta_f = \sqrt{1 - 4\dfrac{m_f^2}{M_\Phi^2}}$ is the fermion velocity, $\vec{n}$ – is the unit vector along the fermion momentum, $\vec{\xi}_1$ and $\vec{\xi}_2$ – are unit vectors directed along the spins of the fermion and antifermion in their rest systems.

Suppose that the fermion pair is transversely polarized ($\vec{\xi}_1 = \vec{\eta}_1$, $\vec{\xi}_2 = \vec{\eta}_2$, $\vec{\eta}_1$ and $\vec{\eta}_2$ are the transverse components of the spin vectors of the fermion pair):

$$(\vec{n}\,\vec{\eta}_1) = (\vec{n}\,\vec{\eta}_2) = 0.$$

In this case, the width of the decay $\Phi \to f + \bar{f}$ is:

$$\frac{d\Gamma(\vec{\eta}_1, \vec{\eta}_2)}{d\Omega} = \frac{N_C g_{\Phi ff}^2 \beta_f}{128\pi^2} M_\Phi \{|a|^2 \beta_f^2 (1 + \vec{\eta}_1\vec{\eta}_2) + |b|^2 (1 - \vec{\eta}_1\vec{\eta}_2)\}. \qquad (7)$$

From this formula it follows that if the transverse polarizations of the fermion pair are parallel $(\vec{\eta}_1\vec{\eta}_2 = 1)$, then the decay of the Φ-boson can occur only due to the CP-even interaction:

$$\frac{d\Gamma(\vec{\eta}_1\vec{\eta}_2 = 1)}{d\Omega} \sim |a|^2 \beta_f^3.$$

The decay of the Φ boson due to CP-odd interaction

can occur only for antiparallel transverse polarizations of the fermion pair $(\vec{\eta}_1\vec{\eta}_2 = -1)$:

$$\frac{d\Gamma(\vec{\eta}_1\vec{\eta}_2 = -1)}{d\Omega} \sim |b|^2 \beta_f.$$
$$(8)$$

If the angle between the transverse polarization vectors of the fermion pair $\vec{\eta}_1$ and $\vec{\eta}_2$ is the φ, then the decay width of the a $\Phi \to f + \bar{f}$ takes the form:

$$\frac{d\Gamma(\vec{\eta}_1, \vec{\eta}_2)}{d\Omega} = \frac{N_C g_{\Phi ff}^2 \beta_f}{128\pi^2} M_\Phi \{|a|^2 \beta_f^2 (1 + \eta_1\eta_2 \cos\varphi) + |b|^2 (1 - \eta_1\eta_2 \cos\varphi) + 2\,\mathrm{Im}(ab^*)\beta_f\eta_1\eta_2 \sin\varphi\}. \qquad (10)$$

In this case, two types of transverse spin asymmetries can arise:

$$A_1 = \frac{1}{\eta_1\eta_2} \frac{d\Gamma(\varphi = \frac{\pi}{2})/d\Omega - d\Gamma(\varphi = -\frac{\pi}{2})/d\Omega}{d\Gamma(\varphi = \frac{\pi}{2})/d\Omega + d\Gamma(\varphi = -\frac{\pi}{2})/d\Omega} = \frac{2\,\mathrm{Im}(ab^*)}{|a|^2 + |b|^2}, \qquad (11)$$

$$A_2 = \frac{1}{\eta_1\eta_2} \frac{d\Gamma(\varphi = 0)/d\Omega - d\Gamma(\varphi = \pi)/d\Omega}{d\Gamma(\varphi = 0)/d\Omega + d\Gamma(\varphi = \pi)/d\Omega} = \frac{|a|^2 - |b|^2}{|a|^2 + |b|^2}. \qquad (12)$$

The transverse spin asymmetry A_1 differs from zero only in the case when the Φ-boson is a mixture of the CP-even and odd states, and this asymmetry can reach values of the order of 1 if the parameters a and b are approximately the same. For a pure CP state, one of the

parameters a and b is zero, then the transverse spin asymmetry A_2 will be either +1 or -1, depending on whether the Higgs boson is a CP-even or an odd particle.

Now suppose that the fermion pair is longitudinally polarized:

131 H.Javid ave, AZ-1143, Baku
ANAS, G.M.Abdullayev Institute of Physics
E-mail: jophphysics@gmail.com

$$(\vec{n}\,\vec{\xi}_1) = \lambda_1, \quad (\vec{n}\,\vec{\xi}_2) = -\lambda_2, \quad (\vec{\xi}_1\vec{\xi}_2) = -\lambda_1\lambda_2,$$

where λ_1 and λ_2 are the helicities of the fermion and antifermion.

The total width of the decay of the Φ boson into a longitudinally polarized fermionic pair is:

$$\Gamma(\lambda_1,\lambda_2) = \frac{N_C\beta_f}{32\pi} g_{\Phi ff}^2 M_\Phi \{[|a|^2\beta_f^2 + |b|^2](1+\lambda_1\lambda_2) + 2\,\mathrm{Re}(ab^*)\beta_f(\lambda_1+\lambda_2)\}. \tag{13}$$

It follows that in the decay of the Φ-boson to the fermionic pair of the helicity of the fermion and antifermion must be the same ($\Phi \to f_R\,\overline{f_R}$ or $\Phi \to f_L\,\overline{f_L}$, where f_R and f_L are right-handed and left-handed polarized fermions). This is due to the conservation of the total angular momentum in the decay $\Phi \to f + \overline{f}$. We determine the degree of longitudinal polarization of the fermion in the decay of $\Phi \to f + \overline{f}$ by formula

$$P_f = \frac{\Gamma(\lambda_1=1)-\Gamma(\lambda_1=-1)}{\Gamma(\lambda_1=1)+\Gamma(\lambda_1=-1)} = \frac{2\,\mathrm{Re}(ab^*)\beta_f}{|a|^2\beta_f^2 + |b|^2}.$$

As can be seen, the degree of longitudinal polarization of the fermion, as well as the transverse spin asymmetries A_1 and A_2, is a source of information about the interference of the CP- even and CP-odd amplitudes in the decay $\Phi \to f + \overline{f}$.

The total width of the decay $\Phi \to f + \overline{f}$, summed over the spin states of the fermion pair, is given by:

$$\Gamma(\Phi \to f\overline{f}) = \frac{N_C\beta_f}{8\pi} M_\Phi\, g_{\Phi ff}^2 [|a|^2\beta_f^2 + |b|^2].$$

According to the MSSM, the coupling constants of the H_{SM}, h, H and A bosons with a fermion pair are determined by the expressions given in Table 1.

Table 1.
The Higgs coupling constants of bosons with a fermion pair in the MSSM

Φ	$g_{\Phi tt}$	$g_{\Phi bb}$
H_{SM}	$\dfrac{m_t}{\eta}$	$\dfrac{m_b}{\eta}$
h	$\dfrac{m_t}{\eta}\dfrac{\cos\alpha}{\sin\beta}$	$-\dfrac{m_b}{\eta}\dfrac{\sin\alpha}{\cos\beta}$
H	$\dfrac{m_t}{\eta}\dfrac{\sin\alpha}{\sin\beta}$	$-\dfrac{m_b}{\eta}\dfrac{\cos\alpha}{\cos\beta}$
A	$\dfrac{m_t}{\eta}ctg\beta$	$\dfrac{m_b}{\eta}tg\beta$

We note that in the table the η is the vacuum value of the standard Higgs boson field

$$\eta = (\sqrt{2}G_F)^{-1/2} = 246\,\mathrm{GeV},$$

G_F is the Fermi constant of weak interactions.

As follows from the decay width (15) and from Table 1, with increasing mass of the Higgs boson M_Φ and fermion m_f the probability of $\Phi \to f + \overline{f}$ decay increases. Because of the smallness of the masses of the electron, muon, u-, d- and s-quarks, the decays $\Phi \to e^- + e^+, \Phi \to \mu^- + \mu^+, \Phi \to u + \overline{u}, \tag{14}$ $\Phi \to d + \overline{d}$ and $\Phi \to s + \overline{s}$ are suppressed. Higgs bosons h, H and A can decay into a pair of $\tau^-\tau^+$-leptons, and a pair of $c\overline{c}$-, $b\overline{b}$-quarks. The heavier H and A-bosons can decay into a pair of t-quarks.

Fig. 3 shows the dependence of the decay widths $\Gamma(H \to t\overline{t})$ and $\Gamma(A \to t\overline{t})$ on the mass of the Higgs boson at a parameter $tg\beta = 3$ and $m_t = 173.2$ GeV. As noted above, with increasing mass of the Higgs boson, the $H \to t\overline{t}$ decay widths increase. In addition, as seen from Fig.3, the width of the decay $A \to t + \overline{t}$ predominates over the width of the decay $H \to t + \overline{t}$.
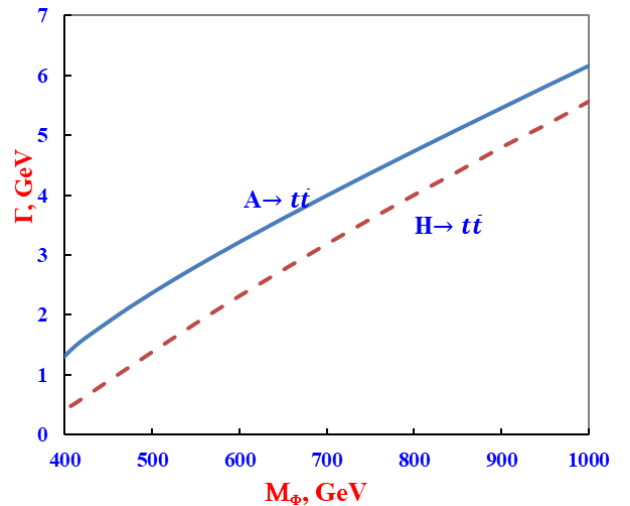

Fig. 3. The dependence of the decay widths $H \to t\overline{t}$ and $A \to t\overline{t}$ on the mass M_Φ

3. THE DECAY OF $H^\pm \to f + \overline{f'}$

The charged Higgs boson can decay into a lepton pair $H^+ \to l^+ + \nu_l$ ($H^- \to l^- + \overline{\nu}_l$) or a quark pair $H^+ \to t + \overline{b}$ ($H^- \to b + \overline{t}$). The Feynman diagram of the decay $H^+ \to f + \overline{f'}$ is analogous to the diagram shown in Fig.2.

According to the MSSM, the matrix element of the decay $H^+ \to f + \overline{f'}$ can be represented in the form:

$$M(H^+ \to f + \overline{f'}) = -\frac{U_{ff'}}{\sqrt{2}\eta} \overline{u}_f(p_1, s_1)[m_f ctg\beta(1 + \gamma_5) + m_{f'} tg\beta(1 - \gamma_5)]v_{f'}(p_2, s_2)H^+(p), \qquad (16)$$

here $U_{ff'}$ is an element of the Kobayashi-Maskawa matrix in the case of the creation of a quark pair $(f\overline{f'} = q\overline{q'})$, and at the production of a lepton pair $U_{ff'} = 1$.

For the Higgs decay width of the boson on the polarized fermionic pair $H^+ \to f + \overline{f'}$ the following expression is obtained:

$$\frac{d\Gamma(\vec{\xi}_1, \vec{\xi}_2)}{d\Omega} = \frac{|U_{ff'}|^2 N_C}{128\pi^2\eta^2} M_{H^+} \sqrt{(1 - r_f - r_{f'})^2 - 4r_f r_{f'}} \times \{[m_f^2 ctg^2\beta + m_{f'}^2 tg^2\beta] \cdot [1 - r_f - r_{f'} - 2\sqrt{r_f r_{f'}}(\vec{\xi}_1\vec{\xi}_2)] -$$

$$- (x_1 - 2r_f - 2\sqrt{r_f r_{f'}})(\vec{n}\vec{\xi}_1)(\vec{n}\vec{\xi}_2)] + [m_f^2 ctg^2\beta - m_{f'}^2 tg^2\beta] \times \sqrt{x_1^2 - 4r_f}[(\vec{n}\vec{\xi}_1) - (\vec{n}\vec{\xi}_2)] - 4m_f m_{f'}\sqrt{r_f r_f'} +$$

$$+ (1 - r_f - r_f')[2m_f m_{f'}(\vec{\xi}_1\vec{\xi}_2) + (x_1 M_{H^+}^2 - 2m_f^2 - 2m_f m_{f'})(\vec{n}\vec{\xi}_1)(\vec{n}\vec{\xi}_2)] - M_{H^+}^2(x_1 - 4r_f)(\vec{n}\vec{\xi}_1)(\vec{n}\vec{\xi}_2)\}. \qquad (17)$$

The notations are introduced:

$$x_1 = \frac{2E_f}{M_{H^+}}, \quad r_f = \frac{m_f^2}{M_{H^+}^2}, \quad r_{f'} = \frac{m_{f'}^2}{M_{H^+}^2}.$$

In the case of the production of a transversely polarized fermion pair $(\vec{n}\vec{\xi}_1) = (\vec{n}\vec{\eta}_1) = 0$, $(\vec{n}\vec{\xi}_2) = (\vec{n}\vec{\eta}_2) = 0$ and the decay width will take the form:

$$\frac{d\Gamma(\vec{\eta}_1, \vec{\eta}_2)}{d\Omega} = \frac{|U_{ff'}|^2 N_C}{128\pi^2\eta^2} M_{H^+} \sqrt{(1 - r_f - r_{f'})^2 - 4r_f r_{f'}} \times \{[m_f^2 ctg^2\beta + m_{f'}^2 tg^2\beta] \cdot [1 - r_f - r_{f'} - 2\sqrt{r_f r_{f'}}(\vec{\eta}_1\vec{\eta}_2)] -$$

$$- 4m_f m_{f'}\sqrt{r_f r_f'} + 2m_f m_{f'}(1 - r_f - r_f')(\vec{\eta}_1\vec{\eta}_2)\} \qquad (18)$$

We determine the transverse spin asymmetry in the decay $H^+ \to f + \overline{f'}$ by the relation:

$$A = \frac{d\Gamma(\vec{\eta}_1\vec{\eta}_2 = 1)/d\Omega - d\Gamma(\vec{\eta}_1\vec{\eta}_2 = -1)/d\Omega}{d\Gamma(\vec{\eta}_1\vec{\eta}_2 = 1)/d\Omega + d\Gamma(\vec{\eta}_1\vec{\eta}_2 = -1)/d\Omega} = = \frac{2\sqrt{r_f r_f'}(1 - r_f - r_{f'} - r_f ctg^2\beta - r_{f'} tg^2\beta)}{[1 - r_f - r_{f'}] \cdot [r_f ctg^2\beta + r_{f'} tg^2\beta] - 4r_f r_{f'}}. \qquad (19)$$

When a longitudinally polarized fermion pair is produced in the decay of $H^+ \to f + \overline{f'}$ the total probability is expressed by the formula

$$\Gamma(\lambda_1, \lambda_2) = \frac{|U_{ff'}|^2 N_C}{32\pi\eta^2} M_{H^+} \sqrt{(1 - r_f - r_{f'})^2 - 4r_f r_{f'}} \{[m_f^2 ctg^2\beta + m_{f'}^2 tg^2\beta] \times$$

$$\times [1 - r_f - r_{f'} + (x_1 - 2r_f)\lambda_1\lambda_2] + [m_f^2 ctg^2\beta - m_{f'}^2 tg^2\beta] \times$$

$$\times \sqrt{x_1^2 - 4r_f}(\lambda_1 + \lambda_2) - 4m_f m_{f'}\sqrt{r_f r_f'} - (1 - r_f - r_f')(x_1 M_{H^+}^2 - 2m_f^2)\lambda_1\lambda_2\}. \qquad (20)$$

We determine the degrees of longitudinal polarization of the t-quark in the decay $H^+ \to t + \bar{b}$ by the formula (with respect to the polarizations b-quark is summed)

$$P_t = \frac{\Gamma(\lambda_1 = 1) - \Gamma(\lambda_1 = -1)}{\Gamma(\lambda_1 = 1) + \Gamma(\lambda_1 = -1)} = \frac{[r_t ctg^2\beta - r_b tg^2\beta]\sqrt{(1 - r_t - r_b)^2 - 4r_t}}{[r_t ctg^2\beta + r_b tg^2\beta](1 - r_t - r_b)^2 - 4r_t r_b} . \tag{21}$$

Figure 4 shows the dependence of the transverse spin asymmetry (19) on the mass of the Higgs boson in the decay of $H^+ \to t + \bar{b}$ at $m_t = 173.2$ GeV, $m_b = 4.88$ GeV and $tg\beta = 3$.
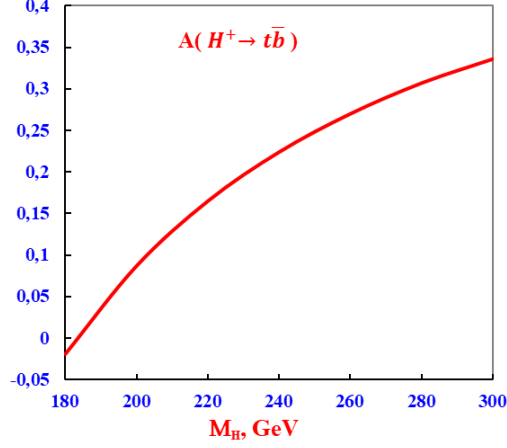
Fig. 4. The dependence of the transverse spin asymmetry on the mass M_{H^+} in the decay $H^+ \to t\bar{b}$.

Figure 5 illustrates the dependence of the degree of longitudinal polarization of the t-quark in the decay $H^+ \to t + \bar{b}$ on the mass of the Higgs boson at $tg\beta = 3$ and $tg\beta = 30$.

Note that using the ATLAS detector in the process of producing a $t\bar{t}$-quark pair in proton-proton collisions at $\sqrt{s} = 7$ TeV the degree of longitudinal polarization of the t-quark was measured [19].
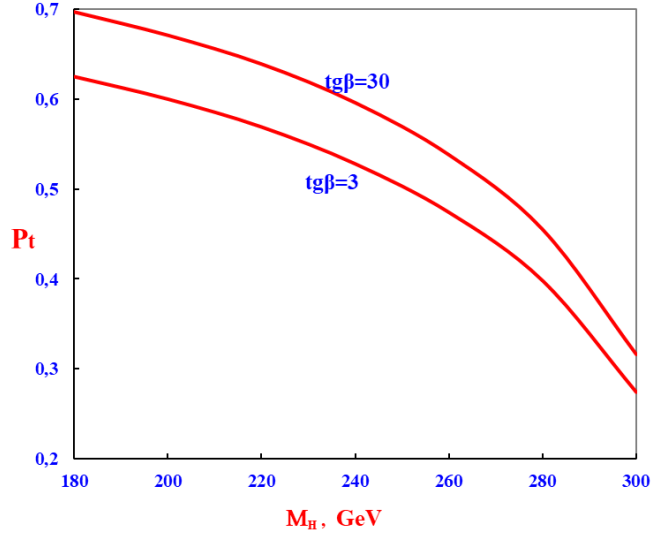

Fig. 5. The dependence of the degree of longitudinal polarization of the t-quark in the decay $H^+ \to t\bar{b}$ on the mass M_{H^+}

The total decay width $H^+ \to t\bar{b}$, summed over the polarization states of the quarks, is:

$$\Gamma(H^+ \to t\bar{b}) = \frac{|U_{tb}|^2 N_C}{8\pi\eta^2} M_{H^+} \sqrt{(1 - r_t - r_b)^2 - 4r_t r_b} \; [(m_t^2 ctg^2\beta + m_b^2 tg^2\beta)(1 - r_t - r_b) - 4m_t m_b \sqrt{r_t r_b}]. \tag{22}$$

27

Fig. 6 illustrates the dependence of the total width of the decay $H^+ \to t\bar{b}$ on the Higgs mass of the boson M_{H^+} at $tg\beta = 3$ and $tg\beta = 30$.

As can be seen, with increasing mass of the Higgs boson, the decay width increases, an increase in the parameter $tg\beta$ also leads to an increase in the width of the decay.
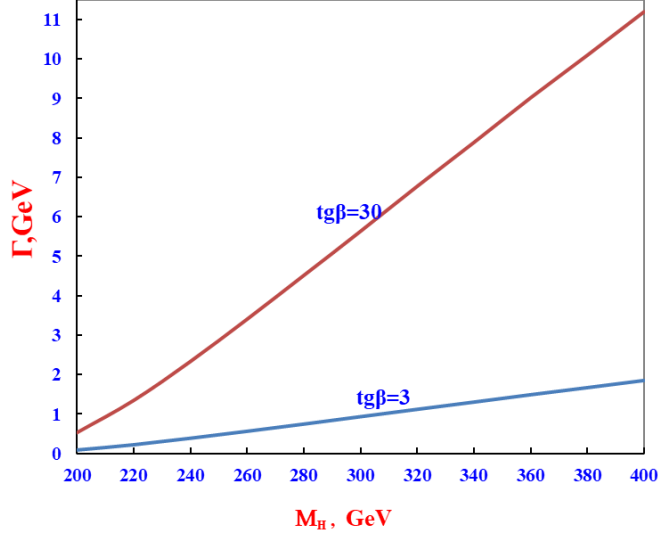

Fig. 6. Dependence of the decay width $\Gamma(H^+ \to t\bar{b})$ on the mass of M_{H^+}

4. THE DECAY OF $H(A) \to t + \bar{b} + W^-$

If the masses of the heavier H and A bosons are slightly less than the masses of the $t\bar{t}$-quark pair $M_H(M_A) < 2m_t$, then they can decay into the real and virtual top quarks:

$$H(A) \to t + \bar{t}^* \to t + \bar{b} + W^-,$$
$$H(A) \to \bar{t} + t^* \to \bar{t} + b + W^+.$$

The decay of $\Phi \to t + \bar{b} + W^-$ (where $\Phi \equiv H$ or A) is described by the Feynman diagram shown in Fig.7. In the MSSM, the matrix element corresponding to this diagram can be written as:

$$M(\Phi \to t\bar{b}W^-) = g_{\Phi tt} \frac{g_w}{2\sqrt{2}} U_\mu^*(k) [\bar{u}(p_1, s_1)\hat{O} \frac{\hat{p} - \hat{p}_1 - m_t}{(p - p_1)^2 - m_t^2 + im_t\Gamma_t} \gamma_\mu(1 + \gamma_5)\upsilon(p_2, s_2)], \qquad (23)$$

where $U_\mu^*(k)$ is the 4-vector polarization of the $W^- -$ boson, g_w is the interaction constant of the W boson with the quark pair $t\bar{b}$, related to the Fermi constant by the relation $\frac{g_w}{8M_w^2} = \frac{G_F}{\sqrt{2}}$, Γ_t is the decay width of the t-quark, and the matrix $\hat{O}$ depends on the scalarity or pseudoscalarity of Φ-boson:

for $\Phi \equiv H$ the $\hat{O}$ is the identity matrix ($\hat{O} = I$), and in the case $\Phi \equiv A$ the $\hat{O} = \gamma_5$.
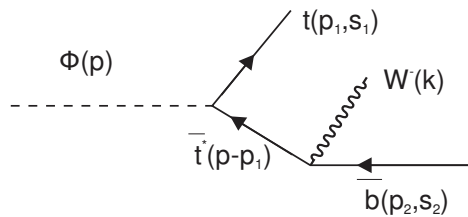

Fig. 7. The Feynman diagram of the decay $\Phi \to t\bar{b}W^-$

After squaring the amplitude of the process $\Phi \to t + \bar{b} + W^-$ we will have:

28

$$\left| M(\Phi \to t\bar{b}W^-) \right|^2 = \frac{g_{\Phi tt}^2 g_w^2}{8M_\Phi^4 [(1-x_t)^2 + r_t\gamma_t]} G_{\mu\nu} I_{\mu\nu}(\Phi \to t\bar{b}W^-), \tag{24}$$

where the notations are introduced:

$$x_t = \frac{2E_t}{M_\Phi}, \quad r_t = \left(\frac{m_t}{M_\Phi}\right)^2, \quad \gamma_t = \left(\frac{\Gamma_t}{M_\Phi}\right)^2,$$

$G_{\mu\nu}$ – is the W boson tensor arising when summing over the polarization states of the vector boson

$$G_{\mu\nu} = \sum_{pol} U_\mu^*(k) U_\nu(k) = -g_{\mu\nu} + \frac{k_\mu k_\nu}{M_w^2}, \tag{25}$$

and $I_{\mu\nu}(\Phi \to t\bar{b}W^-)$ is the quark tensor, which is given in Appendix A.

The product of the W-boson and quark tensors $G_{\mu\nu} I_{\mu\nu}(\Phi \to t\bar{b}W^-)$ is given in Appendix B.

The width of the Higgs boson decay of the $\Phi \to t + \bar{b} + W^-$ channel is expressed by the formula

$$d\Gamma(\Phi \to t + \bar{b} + W^-) = \frac{(2\pi)^4}{2M_\Phi} \left| M(\Phi \to t\bar{b}W^-) \right|^2 \frac{d\vec{k}}{(2\pi)^3 2E_w} \frac{d\vec{p}_1}{(2\pi)^3 2E_t} \frac{d\vec{p}_2}{(2\pi)^3 2E_b} \delta(p - p_1 - p_2 - k). \tag{26}$$

We define the quark spectrum in the case of the production of a longitudinally polarized t-quark. For this, we must take the integral over the phase volume of the vector W-boson. Then the expression for the decay width will have the form:

$$d\Gamma(\Phi \to t + \bar{b} + W^-) = \frac{1}{16(2\pi)^5 M_H} \int \frac{\overline{\left| M(\Phi \to t\bar{b}W^-) \right|^2}}{E_w E_t E_b} d\vec{p}_1 d\vec{p}_2 \delta(M_\Phi - E_t - E_b - E_w), \tag{27}$$

where the bar over the square of the matrix element means that is summed over the polarizations of the $\bar{b}$ - antiquark. Integrating now over the emission angles of t- and b-quarks, for the decay width $\Phi \to t + \bar{b} + W^-$ we obtain expression:

$$\frac{d\Gamma(\Phi \to t + \bar{b} + W^-)}{dx_t dx_b} = \frac{1}{2} \frac{d\Gamma_0(\Phi \to t + \bar{b} + W^-)}{dx_t dx_b} (1 + \lambda_1 P_t) \tag{28}$$

Here

$$\frac{d\Gamma_0(\Phi \to t + \bar{b} + W^-)}{dx_t dx_b} = \frac{g_{\Phi tt}^2 G_F}{32\sqrt{2}\pi^3} \frac{M_\Phi}{(1-x_t)^2 + r_t\gamma_t} f_1 \tag{29}$$

the width of the decay $\Phi \to t + \bar{b} + W^-$ at the creation of polarized quarks, λ_1 is helicity of the t-quark, and P_t is its degree of longitudinal polarization

$$P_t = \frac{f_2}{f_1}, \tag{30}$$

the functions f_1 and f_2 are obtained from the product of the $G_{\mu\nu} I_{\mu\nu}(\Phi \to t\bar{b}W^-)$, tensors given in Appendix B. In the decay of the scalar boson $H \to t + \bar{b} + W^-$ the functions are equal to:

$$f_1 = r_w[x_b(x_t - 4r_t) + (4r_t - 1)(1 - x_w + r_w - r_t - r_b)] +$$

$$+ (1 - x_t + r_t - r_w - r_b)[x_w(x_t - 4r_t) + (4r_t - 1)(1 - x_b + r_b - r_w - r_t)],$$

$$f_2 = r_w \{ \sqrt{x_t^2 - 4r_t} \, [x_b(x_t + \frac{5}{2} - 2r_t) - 2(1 + r_w + r_t - r_b)] +$$

$$+ \frac{x_t}{\sqrt{x_t^2 - 4r_t}} (x_t - \frac{1}{2} - 2r_t)[2(1 - x_w + r_w - r_t - r_b) - x_t x_b] \} +$$

$$+ (1 - x_t + r_t - r_w - r_b)\{ [x_b(x_t + \frac{1}{2} - 2r_t) - x_t - 2(r_b + r_t - r_w)]\sqrt{x_t^2 - 4r_t} +$$

$$+ (x_t - \frac{1}{2} - 2r_t)[2(1 - x_b - r_t - r_w + r_b) - x_t x_w]\frac{x_t}{\sqrt{x_t^2 - 4r_t}} \} ; \tag{31}$$

In the decay of the pseudoscalar boson $A \to t + \bar{b} + W^-$ these functions are given by expressions:

$$f_1 = r_w[x_t x_b - 1 + x_w + r_t + r_b - r_w] + (1 - x_t + r_t - r_w)(x_t x_w - 1 + x_b - r_b + r_t + r_w) ;$$

$$f_2 = r_w[(1 + r_t)x_b \sqrt{x_t^2 - 4r_t} - \frac{x_t r_t}{2\sqrt{x_t^2 - 4r_t}} (2(1 - x_t - x_b - r_w + r_b + r_t) + x_t x_b)] +$$

$$+ (1 - x_t + r_t + r_w - r_b)[(x_t + r_t x_w)\sqrt{x_t^2 - 4r_t} - (x_b - x_w - x_t + x_t x_w + 2(r_w + r_t - r_b))\frac{r_t x_t}{\sqrt{x_t^2 - 4r_t}}] \tag{32}$$

Here $x_b = \dfrac{2E_{\bar{b}}}{M_\Phi}$, $x_w = \dfrac{2E_w}{M_\Phi} = 2 - x_t - x_b$ are the scaling energies of the antiquark $\bar{b}$ - and W -boson,

$$r_w = \left(\frac{M_w}{M_\Phi} \right)^2 , \qquad r_b = \left(\frac{m_b}{M_\Phi} \right)^2 .$$

Figure 8 shows the dependence of the longitudinal polarization degree of the t -quark on the scaling energy x_t at $M_\Phi = 300 \, \text{GeV}$, $x_b = 0,3$ and $M_w = 80.385 \, \text{GeV}$. As follows from the figure, with increasing t -quark energy, the degree of its longitudinal polarization in $H \to t + \bar{b} + W^-$ decay decreases, and in the decay of $A \to t + \bar{b} + W^-$ increases.
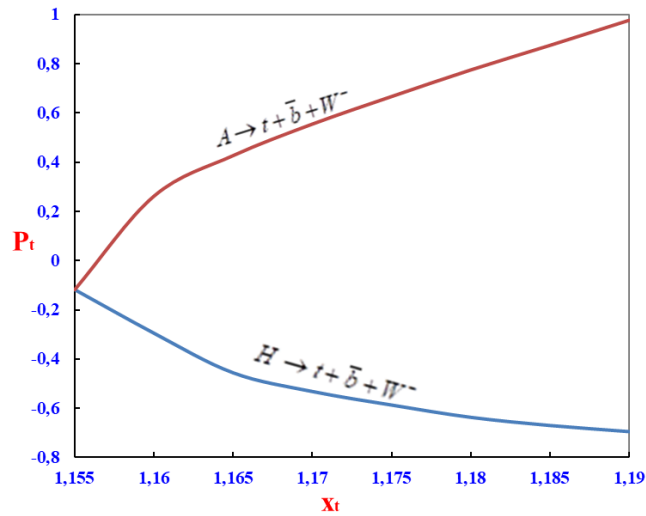

Fig. 8. Energy dependence of the degree of longitudinal polarization of the t -quark

5. THE DECAY OF $H^{\pm} \to b + \bar{b} + W^{\pm}$

If the mass of the charged Higgs boson is $M_{H^{\pm}} < m_t + m_b$, then the decay of this boson into a virtual t-quark and the real b-antiquark is possible, and t-quark can decay into a W^+ vector boson and b is a quark. Thus, one of the possible decays of a charged Higgs boson is the $H^+ \to \bar{b} + t^* \to b + \bar{b} + W^+$ process. This decay is described by the Feynman diagram shown in Fig. 9.
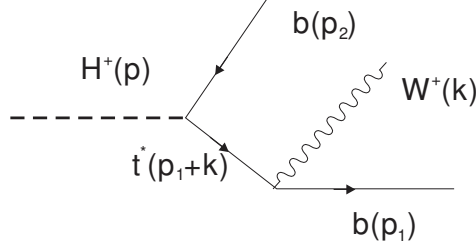

Fig. 9. The Feynman diagram of $H^+ \to b\bar{b}W^+$ decay.

The matrix element of the decay $H^+ \to b + \bar{b} + W^+$ can be represented in the form:

$$M(H^+ \to b\bar{b}W^-) = \frac{g_w}{2\sqrt{2}} \frac{U_{tb}}{\sqrt{2}\eta} U_\mu(k) \times$$

$$\times \bar{u}(p_1)\gamma_\mu(1+\gamma_5) \frac{\hat{p}_1 + \hat{k} + m_t}{(p_1+k)^2 - m_t^2 + im_t\Gamma_t} [m_b tg\beta(1-\gamma_5) + m_t ctg\beta(1+\gamma_5)]\upsilon(p_2).$$

(33)

On the basis of this matrix element for the width of the $H^+ \to b + \bar{b} + W^+$ decay, we have expression:

$$\frac{d\Gamma(H^+ \to b\bar{b}W^+)}{dx_1 dx_2} = \frac{3G_F^2 M_{H^+}^3 |U_{tb}|^2}{32\pi^3[(1-x_2+r_b-r_t)^2 + r_t\gamma_t]} \{m_b^2[tg^2\beta(x_2 - 2r_b) - 2r_t] \times$$

$$\times [r_w(3(1-x_2-r_w)+2r_b) + (1-x_2-r_w)^2] + [m_t^2 r_t ctg^2\beta - m_b^2 tg^2\beta(1-x_2+r_b)] \times$$

$$\times [r_w(1-x_w+r_w-2r_b) + (1-x_1-r_w)(1-x_2+r_w)]\}.$$

(34)

Here x_1 and x_2 are the scaling energies of the quark b and antiquark $\bar{b}$, and r_t, r_b and r_w are given above.

If the mass of a charged Higgs boson is $M_{H^+} > 90$ GeV, then b-quark mass m_b can be neglected in the decay width (34). In this case, the width of the $H^+ \to b + \bar{b} + W^+$ decay is greatly simplified:

$$\frac{d\Gamma(H^+ \to b\bar{b}W^+)}{dx_1 dx_2} = \frac{3G_F^2 M_{H^+} |U_{tb}|^2 m_t^4 ctg^2\beta}{32\pi^3[(1-x_2-r_t)^2 + r_t\gamma_t]} [r_w(x_1+x_2-1) + (1-x_1-r_w)(1-x_2+r_w)].$$

(35)

Integrating this expression with respect to the variables x_1 and x_2, for the total decay width $H^+ \to b + \bar{b} + W^+$ we obtain the expression:

$$\Gamma(H^+ \to b + \bar{b} + W^+) = \frac{3G_F^2 m_t^4 ctg^2\beta}{64\pi^3} M_{H^+} \{\frac{r_w^2}{r_t^3}(4r_w r_t + 3r_t - 4r_w)\ln\frac{r_t - r_w}{r_w(r_t - 1)} +$$

$$+ (3r_t^2 - 4r_t - 3r_w^2 + 1)\ln\frac{r_t - r_w}{r_t - 1} - \frac{5}{2} + \frac{1-r_w}{r_t^2}(3r_t^3 - r_t r_w - 2r_t r_w^2 + 4r_w^2) + r_w(4 - \frac{3}{2}r_w)\}.$$

(36)

This expression of the decay width is valid for a mass of a charged Higgs boson $M_{H^+} < m_t + m_b - \Gamma_t$.

Fig.10 illustrates the dependence of the decay width $\Gamma(H^+ \to b\bar{b}W^+)$ on the mass of Higgs the boson M_{H^+}. It is evident that with an increase in the mass of the charged Higgs boson, the width of its decay along the channel $H^+ \to \bar{b} + t^* \to b + \bar{b} + W^+$ increases from 5.838 MeV to 6.415 MeV, and then monotonically decreases to 0.675 MeV.

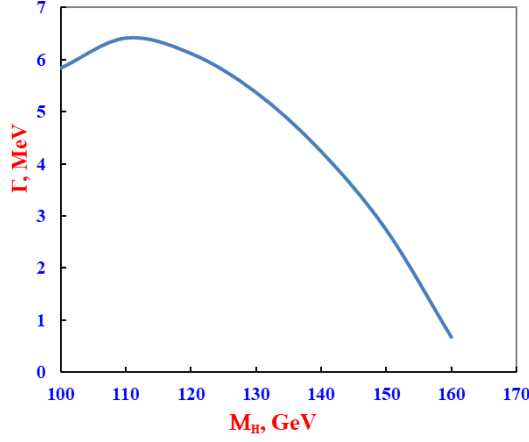*Fig. 10.* The dependence of the decay width $H^+ \to b\bar{b}W^+$ on the mass M_{H^+}

CONCLUSION.

Within the framework of the MSSM, we discussed the decays of neutral and charged Higgs bosons into polarized fermions: $h(H; A) \to f + \bar{f}$, $H^+ \to f + \bar{f}'$, $H(A) \to t + \bar{b} + W^-$ and $H^\pm \to b + \bar{b} + W^\pm$. Analytical expressions for the widths of these decays are obtained, transverse spin asymmetries and the degree of longitudinal polarization of fermions are determined. The dependence of the asymmetries and the widths of the decays on the mass of the Higgs bosons are studied. Numerical calculations are presented in the form of graphs for the decay channels $H(A) \to t + \bar{t}$, $H^+ \to t + \bar{b}$, $H(A) \to t + \bar{b} + W^-$ and $H^+ \to b + \bar{b} + W^+$.

APPENDIX A

Here we give the quark tensor expression in $H \to t + \bar{b} + W^-$ and $A \to t + \bar{b} + W^-$ decays.
In the decay of $H \to t + \bar{b} + W^-$

$$I_{\mu\nu}(H \to t\bar{b}W^-) = 4[(p \cdot p_1) - 2m_t^2][(p, p_2)_{\mu\nu} + m_b(p, s_2)_{\mu\nu}] + +2(4m_t^2 - M_H^2)[(p_1, p_2)_{\mu\nu} +$$

$$+ m_b(p_1, s_2)_{\mu\nu}] + 4m_t(p \cdot s_1)[(p, p_2)_{\mu\nu} + m_b(p, s_2)_{\mu\nu}] + 2m_t[2(p \cdot p_2) - M_H^2 - 2m_t^2] \times$$

$$\times [(s_1, p_2)_{\mu\nu} + m_b(s_1, s_2)_{\mu\nu}] + 8m_t(p \cdot p_1)[(p_2, s_1)_{\mu\nu} + m_b(s_2, p_1)_{\mu\nu}];$$

In the decay of $A \to t + \bar{b} + W^-$

$$I_{\mu\nu}(A \to t\bar{b}W^-) = 4(p \cdot p_1)[(p, p_2)_{\mu\nu} + m_b(p, s_2)_{\mu\nu}] - 2M_A^2[(p_1, p_2)_{\mu\nu} + m_b(p_1, s_2)_{\mu\nu}] +$$

$$+ 4m_t(p \cdot s_1)[(p, p_2)_{\mu\nu} + m_b(p, s_2)_{\mu\nu}] + +4m_t^3[(s_1, p_2)_{\mu\nu} + m_b(s_1, s_2)_{\mu\nu}].$$

We note that $(b, c)_{\mu\nu}$ denotes a brief notation of the tensor

$$(b, c)_{\mu\nu} = b_\mu c_\nu + c_\mu b_\nu - (b \cdot c)g_{\mu\nu},$$

where b and c are arbitrary 4-particle vectors.

APPENDIX _B_

Consider the product of the tensor $G_{\mu\nu} = -g_{\mu\nu} + \dfrac{k_\mu k_\nu}{M_w^2}$ on the tenzor

$$(p, p_2)_{\mu\nu} = p_\mu p_{2\nu} + p_\nu p_{2\mu} - (p \cdot p_2) g_{\mu\nu}:$$

$$(-g_{\mu\nu} + \frac{k_\mu k_\nu}{M_w^2}) \cdot [p_\mu p_{2\nu} + p_{2\mu} p_\nu - (p \cdot p_2) g_{\mu\nu}] = -(p \cdot p_2) - (p_2 \cdot p) + 4(p \cdot p_2) +$$

$$\frac{1}{M_w^2}[(p \cdot k)(p_2 \cdot k) + (p_2 \cdot k)(p \cdot k) - k^2(p \cdot p_2)] = 2(p \cdot p_2) + \frac{2}{M_w^2}(p \cdot k)(p_2 \cdot k) - (p \cdot p_2) =$$

$$= (p \cdot p_2) + \frac{2}{M_w^2}(p \cdot k)(p_2 \cdot k).$$

As a result, for the product of $G_{\mu\nu} I_{\mu\nu}(H \to t\bar{b}W^-)$ tensors in the decay $H \to t + \bar{b} + W^-$ we obtain :

$$G_{\mu\nu} I_{\mu\nu}(H \to t\bar{b}W^-) = 4[(p \cdot p_1) - 2m_t^2] \cdot [(p \cdot p_2) + m_b(p \cdot s_2)] + 2(4m_t^2 - M_H^2) \times$$

$$\times [(p_1 \cdot p_2) + m_b(p_1 \cdot s_2)] + 2m_t[2(p \cdot p_1) - M_H^2 - 2m_t^2] \cdot [(p_2 \cdot s_1) + m_b(s_2 \cdot s_1)] +$$

$$+ 8m_t(p \cdot p_1)[(p_2 \cdot s_2) + m_b(s_2 \cdot s_1)] + \frac{2}{M_w^2}\{4[(p \cdot p_1) - 2m_t^2](k \cdot p) + 2(4m_t^2 - M_H^2)(k \cdot p_1) +$$

$$+ 4m_t(p \cdot s_1)(k \cdot p) + 2m_t[2(p \cdot p_1) - M_H^2 - 2m_t^2](k \cdot s_1) + 8m_t(p \cdot p_1)(k \cdot s_1)\} \cdot [(k \cdot p_2) + m_b(k \cdot s_2)];$$

In the decay of a pseudoscalar $A-$ boson the product of these tensors is given by:

$$G_{\mu\nu} I_{\mu\nu}(A \to t\bar{b}W^-) = 4(p \cdot p_1) \cdot [(p \cdot p_2) + m_b(p \cdot s_2)] - 2M_H^2[(p_1 \cdot p_2) + m_b(p_1 \cdot s_2)] +$$

$$+ 4m_t(p \cdot s_1)[(p \cdot p_2) + m_b(p \cdot s_2)] + 4m_t^3[(s_1 \cdot p_2) + m_b(s_1 \cdot s_2)] + \frac{2}{M_w^2}[4(p \cdot p_1)(k \cdot p) - 2M_H^2(k \cdot p_1) +$$

$$+ 4m_t(p \cdot s_1)(k \cdot p) + 4m_t^3(k \cdot s_1)] \cdot [(k \cdot p_2) + m_b(k \cdot s_2)].$$

_____

[1] _S.Q. Abdullayev._ Standart Model, lepton və kvarkların xassələri, Bakı, <<Zəka print >> ,2017, 274 s.

[2] _A. Djouadi._ The Anatomy of Electro-Weak Symmetry Breaking. Tome I: The Higgs boson in the Standard Model. arXiv: hep-ph/0503172v2, 3 May, 2005.

[3] _P. Langacker._ The Standard Model and Beyond. CRS Press, 2010, 635 p.

[4] _A.A. Sokolov, I.M. Ternov, B.Ch. Zhukovsky, A.V. Borisov._ Gauge fields (Mosk. Gos. Univ. , Moscow, 1986, 260 p., In Russian)

[5] _TaP Cheng, L.F. Li._ Gauge theory of elementary particle physics. Oxford, 1984, 624 p.

[6] ATLAS Collaboration. Observation of a new particle in the search for the Standard Model Higgs boson at the ATLAS detector at the LHC. Phys. Letters, 2012, B 716, p. 1-29.

[7] CMS Collaboration. Observation of a new boson at mass of 125 GeV with the CMS experiment at the LHC Phys. Letters, 2012, B 716, p. 30-61.

[8] _V.A. Rubakov._ UFN, 2012, t.182, № 10, s.1017-1025 (In Russian).

[9] _A.V. Lanev._ UFN, 2014, t. 184, № 9, s. 996-1004 (In Russian)

[10] _D.I. Kazakov._ UFN, 2014, t. 184, № 9, s. 1004-1017 (In Russian)

[11] _A. Djouadi._ The Anatomy of Electro-Weak Symmetry Breaking. Tome II: The Higgs in Minimal Supersymmetric Standard Model. arXiv: hep-ph/0503173v2, 2003.

[12] _J.F. Gunion, H.E. Haber._ Higgs bosons in supersymmetric models (I) Nuclear Phys. 1986, B272, p.1-76.

[13] _J.F. Gunion, H.E. Haber._ Higgs bosons in supersymmetric models (II) Nuclear Phys. 1986, B278, p.449-492.

[14] _S.K. Abdullayev, M.Sh. Gojayev, F.A. Saddigh._ Decay Channels of the Standard Higgs boson. Moscow University Physics Bulletin, 2017, Vol.72, №14, p. 329-339.

[15] *V.A. Marciano, C. Zhang, S. Willenbrock.* Higgs decay to two photons. arXiv: 1109.5304v2, 2011.

[16] M. Shifman, A. Vainshtein, M.B. Volosin, V. Zakharov. Higgs decay into two photons through the W-boson loop. arXiv: 1109.1785v3, 2011.

[17] *S.K. Abdullayev, M.Sh. Gojayev, F.A. Saddigh.* Higgs boson decay channels $H \to \gamma\gamma$, $H \to \gamma Z$, $H \to gg$. Azerbaijan Journal of Physcis, Fizika. 2015, v.XXI, №02, p. 17-22.

[18] *S.K. Abdullayev, M.Sh. Gojayev.* Production and decay of Higgs bosons in muon colliders X International conference "Modern trends in Physics", Baku, 2017, 20-22 April.

[19] *S.F. Hamilton.* Measurement of the longitudinal polarization of the top quark in top-antitop events using the ATLAS detector. CERN− THESIS− 2014-008.

GROWTH OF MWCNTS ON SAPPHIRE SUBSTRATE AS AN INTERMEDIATE LAYER FOR III-V GROUP STRUCTURES

S. ABDULLAYEVA, G. GAHRAMANOVA, T. ORUCOV, R. HASANOV, N. MUSAYEVA, R. JABBAROV

[1]*Institute of Physics, ANAS, Ave. 131 H. Javid, Baku, Azerbaijan*
[2]*Research and Development Center for High Technologies, Ministry of Transport, Communication and High Technologies, Inshaatchilar ave 2, Baku, Azerbaijan*

The main purpose of this paper was using of CNTs as an intermediate layer between sapphire substrate and GaN structures. Therefore, the MWCNTs were deposited on the sapphire substrate with the synthesis of carbon nanotubes done by the aerosol-CVD method. The optimal growth regime was determined from the characterization of CNTs by Raman, SEM and TEM investigations. The investigations showed that the MWCNTs were grown on the substrate horizontally. The inside of tubes was predominantly empty with some of them containing Fe in the tip or on some parts of the walls. The external diameters of the MWCNTs were 25-35 nm.

INTRODUCTION

Applications based on wide bandgap III-V compound semiconductors have rapidly developed over the last several decades due to the ability to apply these semiconductors in high-power, high-frequency electronic and optoelectronic devices [1-4]. Nowadays, biosensors are becoming most important due to their applications in biological and chemical analyses, biomedical, diagnostics, clinical detection, food safety industry, and environmental monitoring. In recent years III-nitride semiconductors have also attracted interest from the scientific community for other applications such as gas and biosensors. Due to their inherent material properties, such as their thermal and chemical stability and biocompatibility, group III-nitrides are a promising material system for the realization of sensitive and stable transducers for biosensor devices. GaN based sensors have been started to study over the last decade (Luther et al., 1999 and Schalwig et al., 2002) and has been studied more and more in recent years [5, 6]. These diverse types of biosensors have been actively pursued by many researchers, using thermometric, piezoelectric, magnetic, and optical transducer approaches [7- 9]. The GaN based optical biosensors are regarded as a promising future real-time biomedical sensor due to the advantages of low temperature drift, low power consumption, low cost, visible radiation application, nondestructive operation, and fast signal generation and reading. Optical biosensors using light absorption of biological elements and photodiode detection have been reported in several studies. Additionally, chemical and other various types of GaN-based (bio)sensors have been started to be investigated during the last decade [10, 11]. The material is chemically stable and inert and, has good optoelectronic properties. GaN also has a large bandgap, therefore the highest occupied and lowest unoccupied orbitals of many biomolecules match very well with it. Taking into consideration all these studies up to now, we can say that III-N materials have a great opportunity to fabricate various types of next generation biosensors. The realization and application of GaInN quantum well heterojunctions as optical transducer elements in chemical sensing and bio-sensing has begun to be demonstrated by many groups since last few years [12-15]. However, large differences in fundamental properties such as lattice constants and thermal expansion coefficients between GaN layer and sapphire substrate generate structural defects and high density of threading dislocations (TD) that leads to deterioration of optical and structural properties.

Carbon nanotubes (CNTs) are innovative nanomaterials due to their high mechanical, thermal and electronic properties (mechanical flexibility, extremely high intrinsic mobility, high thermal conductivity, high elasticity and high optical transmittance) [16-17]. Recently, research groups have been analyzing CNTs to improve the crystal quality of GaN by applying CNT as an intermediate layer between sapphire substrate and GaN buffer layers. Therefore high thermal conductivity, high elasticity and high optical transmittance properties of CNTs make them ideal for electronics devices. In this work, we mainly analyses the impact of CNTs to improve the crystal quality of the GaN structures.

EXPERIMENT

The synthesis processes were carried out by conventional aerosol-chemical vapor deposition (A-CVD) (Fig. 1a) technique (SCIDRE, Germany) which the organic hydrocarbon solvents are used as carbon source. The investigations of MWCNTs/sapphire sample which is grown at optimal growth condition was describe in this paper. This work is based on the injection of the cyclohexane solution in the reactor as an aerosol and its decomposition under high temperature (850ºC). The high frequency (7800 kHz) has been fed in by an ultrasonic device (transducer) to obtain an aerosol from the cyclohexane solutions. Ar/H_2 mixture has flowed to the system during the synthesis process as a transport gas with a total flow ratio 11:1 (constant total flow rate of Argon (Ar) 1100 ml/min and the hydrogen (H_2) 100 ml/min. Argon is the main carrier gas, introduced into the growth chamber. Hydrogen H_2 plays an important role since it controls the growth rate. H_2 was known to have the ability to either accelerate or suppress the formation of carbon.

In general, the process starts by putting Fe covered sapphire substrate in to reactor and the evacuation of the air from quartz reactor using Ar flow for 30 min followed by heating the reactor to 850 °C. Then the aerosol was created from the solution by ultrasonic device with 800 kHz high frequency and was carried by gases to the reactor for CNTs growth. The syntheses proses were continued during 10 minutes and after the synthesis, the reactor always is cooled down under Ar flow. Firstly, the G, D and 2D peaks of the sample was investigated by Raman (Fig. 1b).
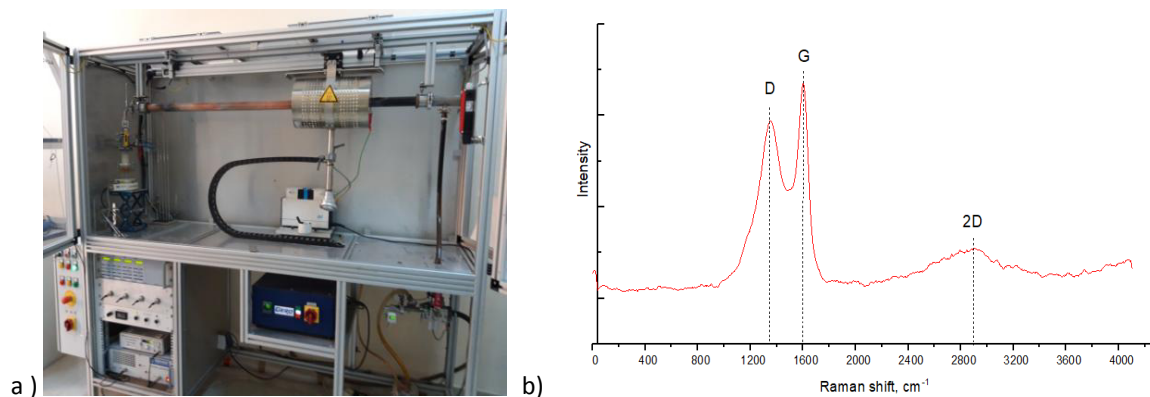
Fig. 1. A-CVD system and Raman characterization of MWCNTs.

RESULTS AND DISCUSSION

The growth of MWCNTs on sapphire mainly studied by scanning electron microscope (SEM) (Fig. 2) and transmission electron microscope (TEM) (Fig. 3). The tubes consist of approximately 25-35 nm diameters. Figure 3 gives the Tem images and present (%) concentrations of only C, O, and Fe as if silicon were absent. Carbon is due to the fact that C surrounds the nano particles so that the TEM electron beam passes through the C shell as well, which generates the C peak in the EDS spectra. The same applies for oxygen. The C signal/percentage can also be due to the presence of CFe3 in the nano particles.
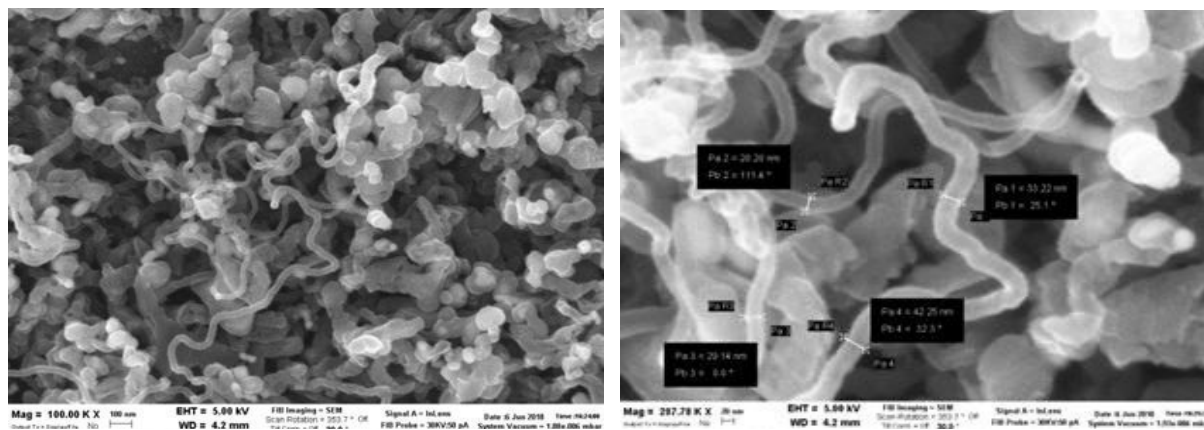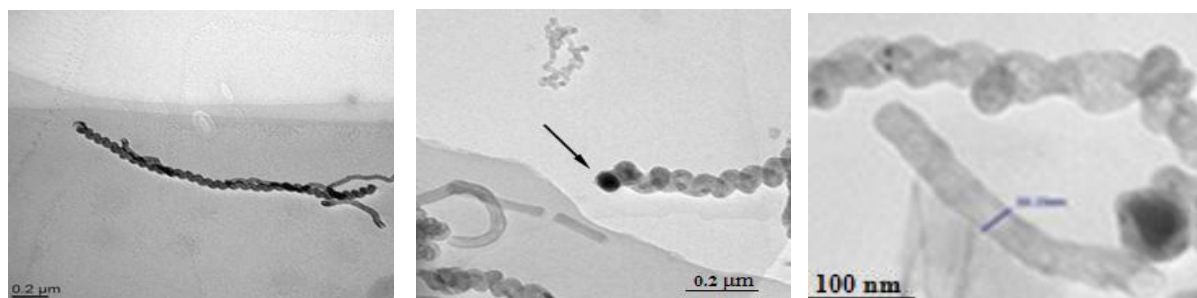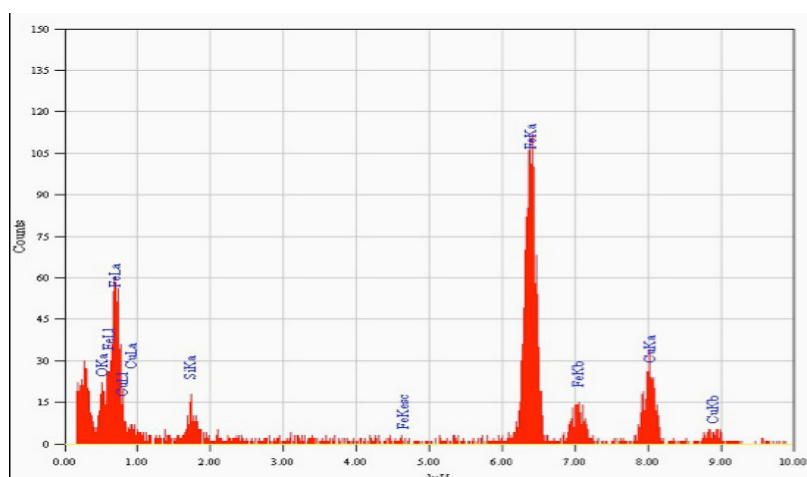

Fig. 2. SEM images of MWCNTs

131 H.Javid ave, AZ-1143, Baku
ANAS, G.M.Abdullayev Institute of Physics
E-mail: jophphysics@gmail.com

Fig. 3. TEM images and EDS spectra of MWCNTs

_____

[1] *S. Nakamura, T. Mukai, M. Senoh.* "Candela-class high-brightness InGaN/AlGaN double-heterostructure blue-light-emitting diodes" Appl. Phys. Lett. 64 (1994) pp. 1687–1689.

[2] *S. Nakamura, S. Pearton, G. Fasol.* "The Blue Laser Diode", Springer (2000) pp. 230–235

[3] *S. Kowsz, E. Young, B. Yonkee, S. Nakamura.* "Using tunnel junctions to grow monolithically integrated optically pumped semipolar III-nitride yellow quantum wells on top of electrically injected blue quantum wells" Optics Express. 25(2017) pp. 3841-3849

[4] *F. Scholz, M. Caliebe, G. Gahramanova, D. Heinz, M. Klein, R.A. Leute , T. Meisch, J. Wang, M. Hocker and*

[5] *K. Thonke.* "Semipolar GaN-based heterostructures on foreign substrates" Phys. Status Solidi B 253 (2016) pp. 13–22 5. *K. H. Baik, J. Kim and S. Jang.* "Improved GaN Based Hydrogen Sensors" ECS Trans 72(5) (2016) pp. 23-28

[6] *F. Ren, B. H. Chu, K. H. Chen, C. Y. Chang, V. Chen, S. J. Pearton.* "GaN Based Sensors" Springer Series in Materials Science 156 (2011) pp. 165-207

[7] *K. Ramanathan, B. Danielsson.* "Principles and applications of thermal biosensors" Biosens Bioelectron 16 (2001) pp. 417–423.

[8] *YR. Chemla, HL. Grossman, Y. Poon et al.* "Ultrasensitive magnetic biosensor for homogeneous immunoassay" Proc Natl Acad Sci USA 97 (2000) pp. 14268–14272.

[9] *AJ. Haes, RP. Van Duyne.* "A nanoscale optical biosensor: sensitivity and selectivity of an approach based on the localized surface plasmon resonance spectroscopy of triangular silver nanoparticles" J Am Chem Soc. 124 (2002) pp. 10596–10604

[10] *N. Chaniotakis and N. Sofikiti.* "Novel semiconductor materials for the development of chemical sensors and biosensors: A review," Anal. Chim. Acta, Vol. 615(2008) pp. 1–9

[11] *I. Cimalla et al.,* "AlGaN/GaN biosensor – Effect of device processing steps on the surface properties and biocompatibility," Sens. Actuators B: Chem., vol. 123 (2007) pp. 740–748

[12] *S.J. Pearton, F. Ren, Y.L. Wang, B.H. Chu, K.H. Chen, C.Y. Chang, W. Lim, J. Lin, and D.P. Norton.* "Recent advances in wide bandgap semiconductor biological and gas sensors", Prog. Mater. Sci., vol. 55 (2010) pp. 1–59.

[13] *K. H. Baik, J. Kim and S. Jang* "Improved GaN Based Hydrogen Sensors" ECS Trans. Vol. 72(5) (2016) pp. 23-28.

[14] *F. Ren, B. H. Chu, K. H. Chen, C. Y. Chang, Victor Chen, S. J. Pearton* "GaN Based Sensors" Springer Series in Materials Science, Vol. 156 (2011) pp 165-207

[15] *D. Heinz, F. Huber, M. Spiess, M. Asad, L. Wu, O. Rettig, D. Wu, B. Neuschl, S. Bauer, Y. Wu, S. Chakrabortty, N. Hibst, S. Strehle, T. Weil, K. Thonke, and F. Scholz,* "GaInN quantum wells as optochemical transducers for chemical sensors and biosensors", IEEE J. Select. Topics Quantum Electron., vol. 23 (2017) pp. 1900109-1–9

[16] *T. H. Seo, A. H. Park, S. Park, Y. H. Kim, G. H. Lee, M. J. Kim, M. S. Jeong, Y. H. Lee,* "Direct growth of GaN layer on carbon nanotube-graphene hybrid structure and its application for light emitting diodes" Scientific Reports 5 (2015) 747 10.1038

[17] *K.S. Kim, et al.* "Large-scale pattern growth of graphene films for stretchable transparent electrodes" Nature 457(2009) pp. 706–710

MODELLING OF COMPONENT AXIAL CONCENTRATION PROFILES IN InSb-GaSb SOLID SOLUTION SINGLE CRYSTALS GROWN BY ZONE MELTING METHOD USING InSb AND GaSb SEEDS

Z.M. ZAKHRABEKOVA, A.I. ALEKPEROV, V.K. KAZIMOVA, G.H. AJDAROV

Institute of Physics of Azerbaijan NAS, AZ 1143, H.Javid ave.,131, Baku, Azerbaijan
E-mail: zangi@physics.ab.az, тел.:(+99412)5393218, Fax: (+99412)4395961

The problem of component concentration distribution in InSb-GaSb solid solution crystals grown by zone melting method using InSb and GaSb seeds is solved in Phann approximation. The component axial concentration profiles in crystals grown in initial macro-homogeneous ingots InSb-GaSb with different composition are calculated taking under consideration the complex change of GaAs segregation coefficient with molten zone composition. It is shown that results obtained by mathematical modeling define the possibilities of zone melting modified method and optimal conditions for growth of InSb-GaSb crystals with given homogeneous and alternative compositions.

INTRODUCTION

The material obtaining with given component axial concentration profile and also the supply of its monocrystallinity are the main tasks of growth process of semiconductor solid solution bulk crystals from melt.

InSb-GaSb system takes the special interest in wide range of semiconductor solid solutions. The component composite of this system is widely used in modern micro- and opto-electronic industry. Besides, InSb and GaSb totally solving in each other in any ratios in both liquid and solid states and form the continuous series of exchange solid solutions [1].

The math task by definition of component distribution along InSb-GaSb solid solution single crystals grown by zone melting modified method with use of seeds from InSb and GaSb is solved in present work in Phann approximation. The aim is the establishment of possibilities of zone melting method for InSb-GaSb single crystal growth with given homogeneous and alternative compositions. The tasks by concentration profile modeling of such type had been solved earlier for Ge-Si crystals and series of semiconductor compounds of A3-B5 type grown up from the melt by different conservative and non-conservative methods [2-9]. The results of these works show the well agreement of the theory with experiment.

The conceptual scheme of InSb-GaSb single crystal growth by zone melting modified method put in the base of math solution of the given task is presented in fig.1. The monocrystalline seed (1) from InSb or GaSb (fig.1A) is put in the low part of cylindrical type crucible. The priori prepared crucibles from InSb (2) and macro-homogeneous solution InSb-GaSb with the given composition are put under the seed. The crucible melting (2) from InSb positioned directly under the seed (fig.1 B) is carried out in vacuum condition. The temperature in boundaries of the melt with the seed and ingot at the moment of recrystallization beginning is equal to InSb melting temperature. The crystal growth takes place on the seed with from the moment of switching mechanism of crucible shift relatively the heater and continues up to total ingot recrystallization.

The task of axial component concentration distribution along InSb-GaSb crystal grown in above mentioned conditions is solved in Phann approximation at which the following conditions are carried out [10]: diffusion rates of InSb and GaSb components in the melt are enough high ones and cause its homogeneity in whole volume; component diffusion in solid phase is negligible one; crystallization front is plane one; there is the equilibrium between liquid and solid phases in crystallization front; GaSb segregation coefficient changes in dependence on the melt composition in the correspondence with phase state equilibrium diagram of InSb-GaSb system; thermal expansion or compression of the material at phase transitions is negligible; the composition of initial polycrystalline ingot InSb-GaSb is macro-homogeneous one.

THEORETICAL CALCULATIONS

Let's introduce the following designations: V_m^0 and V_m are molten zone volumes in initial and current moments; C_c, C_i, C_m are concentration parts of second component (GaSb) in the crystal, initial polycrystalline rod and melt correspondingly; C is general concentration part of GaSb atoms in the melt; C_m^0 is concentration part of GaSb in molten zone in the initial moment; V_c is the melt volume crystallizing per time unit; V_i is the volume of initial ingot InSb-GaSb melting per time unit; $K = C_c/C_m$ is GaSb equilibrium segregation coefficient; L is general length of rod from InSb-GaSb; ℓ is length of material recrystallized part; Z is molten zone length.

Following expressions in these designations are:

$$C_m = \frac{C}{V_m}; \quad \frac{dC_m}{dt} = \frac{\dot{C}V_m - \dot{V}_m C}{V_m^2} \quad \text{and}$$
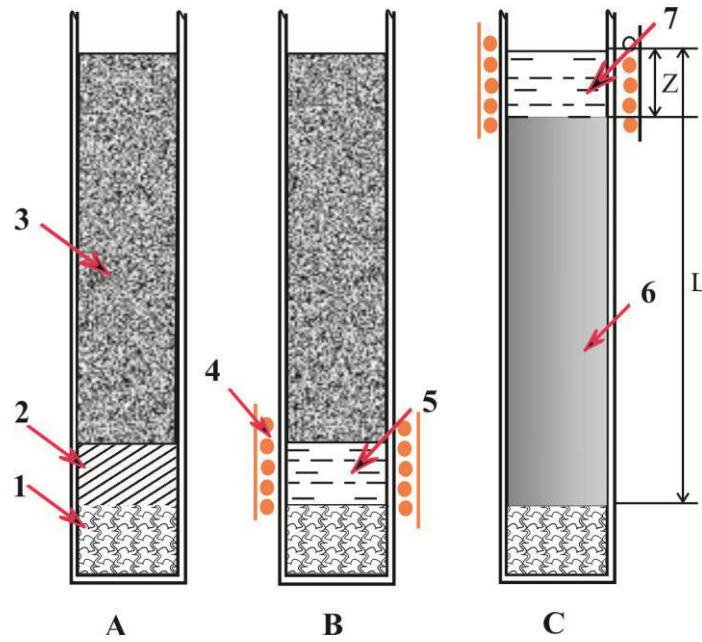
$$V_m = V_m^0 - (V_c - V_i)t \quad (1)$$

Fig.1. The conceptual scheme of InSb-GaSb solid solution single crystals growth by zone melting modified method. A is order of crucible loading; 1, 2 are seed and rod from InSb; 3 is macro-homogeneous rod of InSb-GaSb given composition; B is crystallization starting point; 4 is heater; 5 is melt from InSb; C is moment of final molten zone formation; 6 is InSb-GaSb single crystal; 7 is InSb-GaSb melt; L and Z are lengths of given regions.
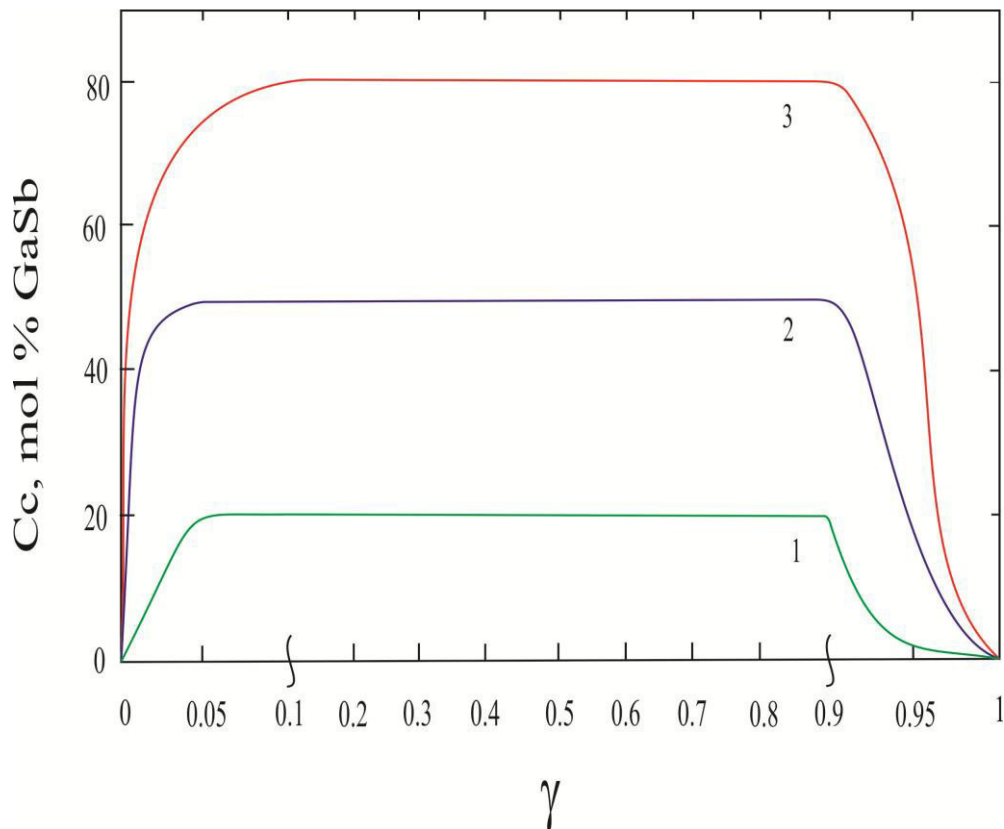

Fig.2. The calculative axial concentration profiles GaSb in InSb-GaSb single crystals grown by zone melting method. The molten zone length is Z=0.1 L. The composition of initial macro-homogeneous ingots InSb-GaSb: 1 – 20, 2 – 50, 3 – 80 at.% GaAs.

By task condition we consider that the melt recrystallization rate (V_c) doesn't depend on time in process of whole technological cycle and Z and V_i parameter values stay unchangeable ones up to the moment of final molten zone formation. In this case the following equations are equal in region of crucible with L-Z length from the seed (fig.1):

$$V_m = V_m^0 \; ; \quad C_m^0 = 0; \quad V_i = V_c \qquad \text{and}$$

$$\dot{C} = V_i C_i - V_c C_m K \qquad (2)$$

Taking under consideration (2) from equations (1) we have the division of alternatives and integration after series of transformations:

$$\int_0^{C_m} \frac{dC_m}{C_i - C_m K} = \frac{V_c t}{V_m^0} = \frac{l}{Z} \qquad (3)$$

We have from the moment of final molten zone formation of Z length:

$$V_m = V_m^0 - V_c t \;\; , \; \dot{V}_m = -V_c, \; \dot{C} = -V_c \, C_m K \quad (4)$$

Taking under consideration (4) we obtain after series of transformations and integration:

$$\int_{C_{mf}^0}^{C_m} \frac{dC_m}{C_{mf}^0 - C_m k} = \ln \frac{V_m^0}{V_m^0 - V_c t} \qquad (5)$$

Here C_{mf}^0 is initial concentration part of GaSb in the melt in moment of final molten zone formation. Let's write the equation (5) in the following form designated the length and part of melt crystallized part ($V_c t / V_m^0$) in t moment by l^* and γ symbols correspondingly:

$$\gamma \equiv \frac{l^*}{Z} = 1 - \exp\left[-\int_{C_m}^{C_{mf}^0} \frac{dC_m}{C_m K - C_m} \right] \qquad (6)$$

The definition of l/Z and γ as C_m function is the same as $C_c = K \, C_m$ along whole material length treated by zone crystallization requires the integral solution in equations (3) and (6) in which the segregation coefficient of second component (K) depending on C_m is included. It is known that K value in InSb-GaSb system changes enough difficultly in wide limits in dependence on melt composition [1]. This circumstance leads to the necessity of calculations of integrals in (3) and (6) by numerical method by the way of $K = C_c / C_m$ conjugated values in corresponding intervals of C_m change on data of system equilibrium phase state diagram.

The character curves of GaSb concentration distribution by solid solution crystal lengths InSb-GaSb calculated from equations (3) and (6) and relation $C_c = C_m K$ are presented in fig.2. The calculations are carried out for three different values C_i (x=0.2; 0.5; 0.8) of InSb-GaSb initial ingot at molten zone length Z=0,1L. As it is seen from fig.2, GaSb concentration in initial part of all crystals increases on the length from zero up to corresponding value C_i of initial homogeneous ingot InSb-GaSb. Further, C_c value with crystal growth stays constant up to final zone formation by length Z=0.1 L. In this part of ingot GaAs concentration begins to decrease with l increase and tends to zero at l=L. The length of initial part with GaSb increasing concentration and final one with GaSb decreasing concentration is similar for all samples and is equal to molten zone length Z=0.1 L. Note that the enough strong increase of GaSb concentration in these parts of all ingots which causes the big output of solid solution single crystals with homogeneous composition is of great interest.

CONCLUSION

The curve family (fig.2) demonstrates the potential and availability of zone melting method for growing of InSb-GaSb solid solution single crystals with given homogeneous and alternative compositions. Summarizing the above mentioned one can state the following. The mathematical modeling of component axial concentration distribution along InSb-GaSb crystals grown up by zone melting method with use of seeds from InSb and GaSb allows us to estimate the optimal technological parameters for single crystal obtaining of this system with given distribution and component concentration.

_____

[1] *V.S. Zemskov, V.B. Lazarev.* Tverdie rastvori v poluprovodnikovix sistemax, «Nauka», Moskva, (1978) 197. (In Russian).

[2] *T.A. Campbell, M. Schweizer, P.Dold et al..* Float zone growth and characterization of Ge1-xSix (x<10 at%)single crystals, J. Crystal Growth, 226 (2001) 231-237.

[3] *N.V. Abrosimov, S.N. Rossolenko, Thieme W. et al..* Czochralski growth of Si- and Ge-rich SiGe single crystals, J. Crystal Growth, 174 (1997) 182-186.

[4] *G.Kh. Azhdarov, T. Kucukomeroglu, A. Varilci et al..* Distribution of components in Ge-Si bulk single crystals grown under continuous feeding of the melt with the second component (Si), J. Crystal Growth, 226 (2001) 437-442.

[5] *G.Kh. Azhdarov, R.Z. Kyazimzade.* Growth of homogeneous single crystals of Ge-Si solid solutions by the modified Bridgman method, Crystallography Reports, 50 (2005) S149-S153.

[6]   *G.Kh. Azhdarov, Z.M. Zeynalov, Z.A. Agamaliyev, A.I. Kyazimova.* Growth of single crystals of semiconductor solid solutions by double feeding of the melt method, Crystallography Reports, 55 (2010)763-767.

[7]   *Z.M. Zaxrabekova.* Kristalli tverdix rastvorov Ge-Si. Poluchenie i elektricheskie svoyststva slojnoleqirovannix kristallov Ge-Si s primesyami medi, alyuminiya i surmi, LAP LAMBERT Academic Publishing, Германия (2013) 139. (In Russian).

[8]   *V.K. Kazimova.* Kristalli Ge-Si i ix svostva. Poluchenie i elektricheskie svoystva tvyerdix rastvorov Ge-Si, slojnoleqirovannix primesyami medi, indiya i surmi, LAP LAMBERT Academic Publishing, Германия (2013) 144. (In Russian).

[9]   *Kostylev, J.K. Woodacre, Y.P. Lee et al.,* Melt zone growth of Ge-rich Ge1-xSix bulk single crystals, J. Crystal Growth, 377 (2013)147-157.

[10]   *V.M. Glazov, V.S. Zemskov.* Fiziko-ximicheskie osnovi leqirovaniya poluprovodnikov. M.: Nauka, (1967) 371. (In Russian).

PINNING ENERGY OF $Bi_2Sr_2CaCu_2O_X$ AND $Bi_2Sr_2Ca_{0.8}Zn_{0.2}Cu_2O_X$

S.S. RAGIMOV, G.I. AGAYEVA

Institute of Physics of Azerbaijan National Academy of Sciences H.Javid ave., 131, AZ-1143, Baku, Azerbaijan
e-mail: sadiyar@mail.ru

The superconducting $Bi_2Sr_2CaCu_2O_X$ and $Bi_2Sr_2Ca_{0.8}Zn_{0.2}Cu_2O_X$ which was obtained by solid-state synthesis method was investigated. The pinning energy was estimated according the magnetic field dependence of specific resistivity. It was observed that, the Zn substitution of Ca leads to increase of the pinning energy.

Keywords: pinning energy, superconducting material, specific resistivity, coherence length, magnetic field dependence
PACS:74.62.Bf; 74.25.F; 74.40.-n

INTRODUCTION

For a wide practical application of superconducting materials, it is necessary high critical temperature and high conductive capacity. The critical current density is one of the critical parameters that limit the existence of superconductivity. The study of current transfer processes is also of interest from a physical point of view, since it allows one to obtain additional information on some parameters of the superconducting state. The magnitude of the critical current is highly dependent on the conditions and technology of manufacturing high-temperature superconductor [1-8].

In superconductors of the second kind, the pinning effect plays a large role. The values of the critical current density (j_c) in second-type superconducting materials are directly dependent on the ability to move vortices and pinning centers. Pinning flow is always enhanced with increasing sample heterogeneity [8-13]. In the case of Bi-based HTSCs, it can be assumed that such centers may be phase boundaries, superstoichiometric concentrations of Ca and Cu, and others impurities [2,4,5,11].

In the present work we analyzed the pinning energy of $Bi_2Sr_2CaCu_2O_X$ and $Bi_2Sr_2Ca_{0.8}Zn_{0.2}Cu_2O_X$ polycrystalline samples.

EXPERIMENTAL RESULTS AND THEIR DISCUSSION

The investigated $Bi_2Sr_2CaCu_2O_X$ and $Bi_2Sr_2Ca_{0.8}Zn_{0.2}Cu_2O_X$ was synthesized by solid-state synthesis method. Samples were prepared from stoichiometric amounts of high-purity Bi_2O_3, $CaCO_3$, $SrCO_3$, ZnO and CuO powders. First, refractory components ($CaCO_3$, $SrCO_3$, and CuO) taken in a desired proportion were sintered at 1173-1243K for 20-50 h and then Bi_2O_3 and ZnO were added. The solid state reaction of the mixed and pressed powders was performed at 1100-1135K in air for 50h applying intermediate grindings. Cooling was carried out with a rate of 1.5^0C/min.

The phase purity of the obtained samples was investigated by X-ray analyses. The XRD analysis was performed using a Brucker -D8 advance diffractometer at room temperature. The X-ray diffractogram of $Bi_2Sr_2CaCu_2O_X$, $Bi_2Sr_2Ca_{0.8}Zn_{0.2}Cu_2O_X$ are shown in fig.1. According the x-ray data $Bi_2Sr_2CaCu_2O_X$ and $Bi_2Sr_2Ca_{0.8}Zn_{0.2}Cu_2O_X$ can be called single phase. One can see from fig.1, the additional peaks are observed for the Zn-doped compound. From the XRD data, various structural characteristics such as, lattice parameter: a=5,396; b=5,395; c=30,643, V=892.06 $Å^3$, system-orthorhombic, space group Pnnn for $Bi_2Sr_2CaCu_2O_X$ and $Bi_2Sr_2Ca_{0.8}Zn_{0.2}Cu_2O_X$ were deduced.
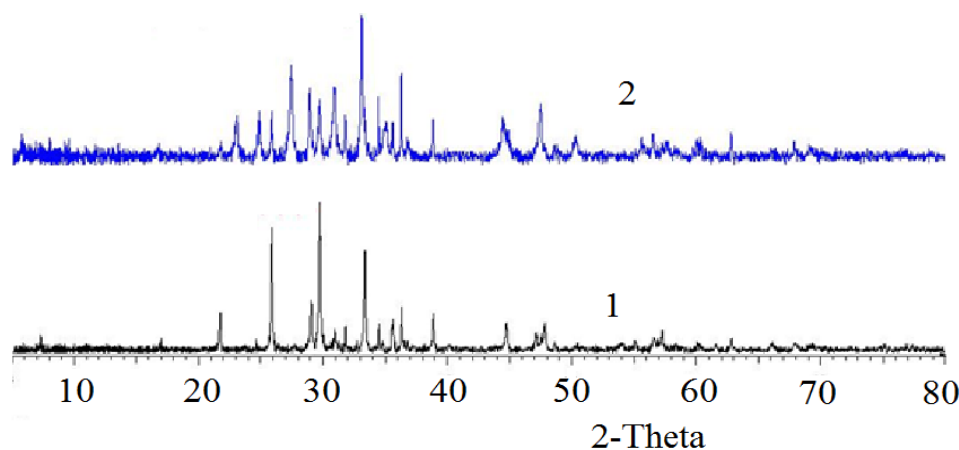
Fig. 1. The X-ray diffractogram of $Bi_2Sr_2CaCu_2O_X$, $Bi_2Sr_2Ca_{0.8}Zn_{0.2}Cu_2O_X$.

To calculate the pinning energy, we used the temperature dependences of the resistivity at various values of the magnetic field [14].

Figure 1 shows the dependence of the activation energy U$_p$ on the external magnetic field for the investigated samples.

At present, the nature of pinning centers in HTSCs has not been finally established, but it is clear that the relatively weak pinning of vortexes in these materials is due to the low energy U$_p$ of the fluxoid bond at the pinning center due to the small coherence length ξ. It is known that pinning is most effective in a separate vortex line [8,9,11]. Pinning flow is always enhanced with increasing sample heterogeneity. In this case, the replacement of the element of calcium by zinc leads to the formation of defects in the crystal structure. The result is an increase in pinning energy.

To evaluate U$_0$, you can use the expression [10,11]

$$U_0 = \beta B_c^2 \xi \phi_0 / B \qquad (1)$$

where B$_c$ is a thermodynamic critical field, ϕ_0 - flow quantum(ϕ_0=2.07.10^{-15}Tl.m^2), β = 1 is the number coefficient. As can be seen from (1), a decrease in ξ leads to a drop in U$_0$.

As can be seen, to determine the pinning energy, it is necessary to know the upper critical magnetic fields and the coherence length. The upper critical magnetic fields and the coherence length values were experimentally determined from the dependence of the resistance on the magnetic field [5,14]. In the low-temperature region of the resistive transition to the superconducting state, the pinning energy of Abrikosov vortices U$_p$ is significantly higher than the thermal energy (U$_p$ >> kT). In this region, the resistance is determined by thermally activated motion

of the magnetic flux and is expressed by the well-known Arrhenius law [6-8].

$$\rho = \rho_0 \cdot exp\left(-U_0/k_B T\right) \qquad (2)$$

The pinning energy U$_p$ was calculated for fixed magnetic fields from the slope of the linear sections of the dependences ln (ρ/ρ$_0$) = f(1/T). The obtained values of U$_p$ for investigated samples are presented in fiq.1.

As can be seen from fig.1, the pinning energy decreases with increasing magnetic field in investigated samples. Note that the rate of decrease in the activation energy U$_p$(B) also slows down. Apparently, this dependence U$_p$(B) is caused by the saturation of the activation energy in strong fields and at low temperatures, where the effects of magnetic flux movement become less significant. As can be seen, U$_0$ for the sample Bi$_2$Sr$_2$Ca$_{0.8}$Zn$_{0.2}$Cu$_2$O$_X$ (with the addition of Zn element) is higher than in the Bi$_2$Sr$_2$CaCu$_2$O$_X$. In our opinion, this is due to the different nature of the pinning centers in these materials: point defects, the presence of other phases. Structural defects that occur in complex HTSC materials serve as an effective pinning center for magnetic flux lines [12]. The presence of impurities and phases in HTSCs leads to a local decrease in the Gibbs free energy of vortex lines. If these defects can lead to a change in the superconducting order parameter, then the flux lines will pinning efficiently. The degree of variation of the superconducting order parameter is approximately equal to the radius of the normal part of the vortices, or the coherence length. Therefore, in order to understand the effect of pinning flow lines, it is very important to know the coherence length with respect to the sizes of defects. These intrinsic superconducting properties can be determined from measurements of the temperature dependence of the second critical magnetic field.
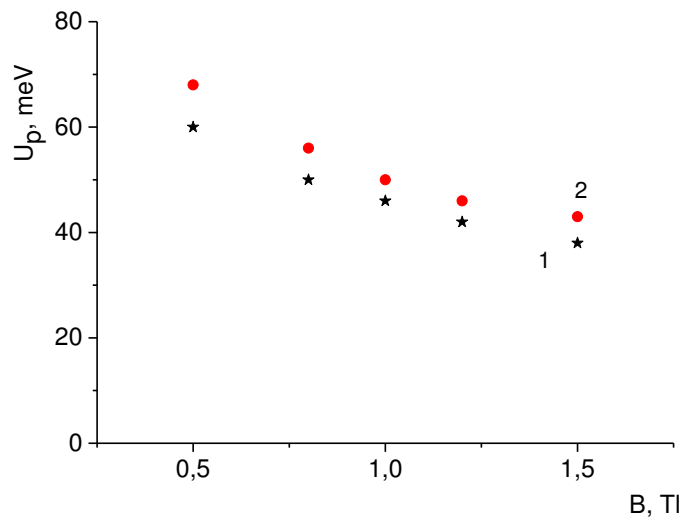

Fig. 2. The magnetic field dependence of pinning energy of Bi$_2$Sr$_2$CaCu$_2$O$_X$ (1) and Bi$_2$Sr$_2$Ca$_{0.8}$Zn$_{0.2}$Cu$_2$O$_X$(2)

The replacement of Ca with Zn leads to the formation of defects in the crystal structure of the sample. Moreover the resistance of the samples may increase either by increasing the number of defects or by decreasing the density of charge carriers. It is possible that in this case both mechanisms take place. The defects in the crystal structure as a result of the introduction of the element Zn, lead to additional pinning centers. And this in turn increases the pinning energy of the whole in the sample.

Note that when replacing calcium with zinc, the lattice parameter decreases. This is due to the fact that zinc has a smaller ionic radius than calcium (1.04 Å and 0.83 Å, respectively). In this case the crystal structure deforms, similar to that arising under external pressure, as a result of which the lattice parameter decreases.

CONCLUSION

The replacement of Ca with Zn leads to the formation of defects in the crystal structure of the superconducting $Bi_2Sr_2Ca_{0.8}Zn_{0.2}Cu_2O_X$. The pinning energy was estimated according the magnetic field dependence of specific resistivity. It was observed that, the Zn substitution of Ca leads to increase of pinning energy.

_____

[1] *I. Askerzade,* Unconventional Superconductors: Anisotropy and Multiband Effects, Springer, Berlin, Heidelberg, (2012).

[2] *S.I. Bondarenko, V.P. Koverya, A.V. Krevsun, and S.I. Link.* High-temperature superconductors of family $(RE)Ba_2Cu_3O_{7-\delta}$ and their application (Review Article), FNT, v.43, №10, p.1411-1445, (2017).

[3] *S.S. Ragimov, I.N. Askerzade.* Thermoelectromotive force in $Bi_2Sr_2Ca_2Cu_4O_{11}$ bismuth-based high-temperature superconductor, Technical Physics 55, №10, p.1538-1539, (2010).

[4] *V.A. Alekseev, V.A. Karetnikov, D.A. Lapshin et.all.,* The influence of synthesis technology of Bi-Pb-Sr-Ca-Cu-O ceramics on the superconducting properties, Superconductivity: physics, chemistry, technical v.3, №8, c.1678-1684, (1990).

[5] *S.S. Ragimov, A.A. Saddinova, V.M. Aliev, R.I. Selim-zade.* The influence of fluctuations on the superconducting properties of $Bi_2Sr_2Ca_{0.6}Zn_{0.4}Cu_2O_X$ and $Bi_2Sr_2Ca_1Cu_2O_X$, Materials Science Forum, v. 845, p. 17-20, (2016).

[6] *M. Pekala, H. Boigrine and M, Ausloss.* Electrical and thermomagnetic effects in $Bi_{1.7}Pb_{0.3}Sr_2Ca_2Cu_3O_{10}$ superconducting ceramics, J.Phys.Condens.Matter., №7, p.5607-5621, (1995).

[7] *M. Pekala, K. Kitazava, A. Polaczek et al.* Anisotropy thermoelectric power and thermal conductivity in superconducting single crystals Bi-Ca-Cu-O, Solid State Communations, , v.76, №3, p.419-421, (1990).

[8] *A.I. Ponomarev, K.R. Krilov, N.V. Mushnikov et all.,* Paraconductivity, critical fields and activasion energy in $Bi_2Sr_2CaCu_2O_{8+X}$ ceramics, Superconductivity: physics, chemistry, technical v.5, №12, p. 2259-2271, (1992).

[9] *U. Welp, W. Kwok, G. Grabtree et al.,* Magnetic measurements of the upper critical field of $YBa_2Cu_3O_{7-X}$ single crustals, Physical Review Letters, v.62, №16, p.1908-1911, (1989).

[10] *N.R. Werthamer, E. Helfand, P.C. Hohenberg.* Temperature and Purity Dependence of the Superconducting Critical Field, Hc2. III. Electron Spin and Spin-Orbit Effects, Phys.Rew., v.147, No1, p.295-302, (1966).

[11] *E.A. Pashichkiy, V.I. Vakaryuk.* Pinning Abrikosov vortices on dislocations and critical current in high-temperature superconductors, FNT, т.28, №1, p.16-23, (2002).

[12] *M. Lan, J. Liu, Y. Jia et al.* Resistivity and upper critical field of $YBa_2Cu_{3-X}Fe_XO_{7-Y}$ single crystals, Physical Review B, 1993, v.47, №1 p.457-462.

[13] *A.V. Samochvalov, A.S. Melnikov.* Microscopic theory of pinning multi-quantum swirl in cylindrical cavity, JETP, Vol. 126, No 2, (2018).

[14] *S.S. Ragimov, G.I. Agayeva.* The magnetic field influence on the specific resistivity of Bi2Sr2CaCu2OX film in the superconducting transition region, Transactions of Azerbaijan National Academy of Sciences, physics and astronomy v. XXXVIII, № 5 p.96-99, (2018).

REVIEW OF INTERACTION CONSTANT OF VECTOR MESON-NUCLEON IN THE FRAMEWORK OF AdS/QCD HARD WALL MODEL

Sh. MAMMADOV, Sh. TAGIYEVA

Instittute of Physical Problems and Theoretica Physics Department, Baku State University,
Z.Khalilov str.,23, 1048,Baku, Azerbaijan
e-mail: sh.mamedov62@gmail.com, shahnaz.ilqarzadeh.92@mail.ru

In the framework of AdS/QCD hard wall model ρ meson-nucleon interaction constant is calculated by us. Langrangian interaction is used between spinor, vector and pseudo-scalar fields in the internal part of AdS space. Using AdS/QCD correspondence principle the integral expression for meson-nucleon interaction constant is obtained and its numerical value is calculated.

INTRODUCTION

Last time the study of elementary cells in AdS/QCD models presents the big inteterst in theoretical physics.

The AdS/QST duality idea is formed from supersymmetric theory. The supersymmetric theory combines 4 fundamental interactions: gravitational, electromagnetic, weak and strong ones. This duality requires the equivalence of 2 below mentioned theories: the theory of 4-dimensional calibration and the theory of 5-dimensional AdS space-gravitation.

Gauge theory describes the other interaction forces: electromagnetic, weak and strong ones excluding the gravitation forces. For example, *U(1)* electromagnetic and *SU(3)* strong interactions are described by Gauge theory (this theory is called quantum chromodynamics, QCD).

De-Sitter space is the solution of constant positive Einstein curve. AdS (anti- De-Sitter space) is constant negative curve of time space. AdS/QST compatibility forms the connection between 4- and 5-dimensional physics. This theory is callede gollographic one.

The interaction of elementary cells is calculated by 2 AdS/QST models. The hard wall model in this model sets the boundary conditions at the points 0 and z_m at z spatial variable and thus, the theory in limit region is established.

The additional region called Dilaton $D(z)=\lambda^2 z^2$ multiplied on $e^{D(z)}$ Langrangian limit is added to soft wall model.

The meson-nucleon interaction is studied in this article on the base of AdS/QCD hard wall model. This problem has been considered in the previous articles [4,7,8]. However, the gluon condensate in these cases isn't considered in X pseudoscalar region. The constant coefficient ρNN defined in the work [1] is recalculated by X field application.

HARD WALL MODEL

The interaction expression in hard wall model is given bellow and changes in interval:

$$S_{q/t}(V(q,z)) = \int d^4x \, dz\sqrt{g} \, \mathcal{L}_{q/t} \qquad (1)$$

$g=|det g_{MN}|$ (M,N =0,1,2,3,5) changes at interval $0 \leq z \leq z_m$. $\mathcal{L}_{q/t}$ is Langrangian interaction between vector and fermionic fields inside AdS space. AdS space metric is given in Poincare coordinates:

$$ds^2 = \frac{1}{z^2}\left(-dz^2 + \eta_{\mu\nu}dx^\mu dx^\nu\right)$$

$\eta_{\mu\nu}$ is 4D Minkovski metric

$$\eta_{\mu\nu} = \text{diag}(1,-1,-1,-1).$$

The pseudoscalar field X is added in theory of golographic duality inside AdS space $SU(2)_L \times SU(2)_R$ besides vector and fermionic fields with the aim of providing of chiral symmetry breakaging by Higgz mechanism.

$$S_{5D} = \int d^4x \int dz \sqrt{G} \, Tr[|DX|^2 + 3X^2]$$

Here, $|DX|^2 = (D_M X)^\dagger (D^M X)$, $D_M X$ is covariant variative and is defined by following way:

$$D_M X = \partial_M X - iL_M X + iR_M X.$$

The asymptotic solution for X in $z \to 0$ value is given below:

$$X(z) \approx \frac{1}{2}am_q z + \frac{1}{2a}\sigma z^3 = v(z). \qquad (2)$$

Here m_q and d are quark aggregation and σ is chiral condensate value. m_q and σ are fixed in the result of solution of ultraviolet and IR limits according to pseudoscalar region X. $mq = 0.0083$ GeV , $\sigma = (0.213)3$ GeV3 and $a = Nc/(2\pi)$ [1].

The following expression:

$$f_{1L}^n = c_1^n z^{\frac{5}{2}} \mathcal{J}_2(pz), \quad f_{1R}^n = c_1^n z^{\frac{5}{2}}\mathcal{J}_3(pz),$$
$$f_{2L}^n = -c_2^n z^{\frac{5}{2}}\mathcal{J}_3(pz), \quad f_{2R}^n = c_2^n z^{\frac{5}{2}}\mathcal{J}_2(pz). \quad (3)$$

is described in work [7] for nucleon profil function in hard wall model. In (3) formula the normalization constants

$$\int_0^{z_m} \frac{dz}{z^5} f_{1L}^{(n)}(z) f_{1L}^{(m)}(z) = \delta_{nm} , \qquad (4)$$

and in (4) formula the obtained normalization conditions are given below:

$$|c_{1,2}^n| = \frac{\sqrt{2}}{z_m \, \mathcal{J}_2(m_n z_m)}. \qquad (5)$$

INTERNAL INTERACTION CONSTANT AND $g_{\rho NN}$ MESON-NUCLEON INTERACTION

According to AdS/QSD the formation inside 4D in QSD in functional 5D space AdS_5 is defined by following way:

$$Z_{KXD}(V_\mu^0) = e^{iS_{q/t}(\tilde{V}_\mu(q,z))} \qquad (6)$$

Here $\tilde{V}_\mu^0(q,z)$ is vector field in 5D AdS space;

$\tilde{V}_\mu^0 = \tilde{V}_\mu(q, z=0) = V_\mu(q)$

is 5D space value $\tilde{V}_\mu^0(q,z) = V_\mu^0(q)V(q,z)$ of $(V(q,z=0)=1)$ vector field. By other hand, it is known that AdS functionality of 4D vector current converter for nucleons in space boundary is equal to functional converter according vacuum unite of 4D field in ultraviolet boundary.

$$<J_\mu> = -i\frac{\delta Z_{KXD}}{\delta \tilde{V}_\mu^0}\Big|_{\tilde{V}_\mu^0=0} \qquad (7)$$

Here J_μ being the vector current for nucleons at ρ meson-nucleon interaction is expressed by following way (8):

$$J_\mu(p',p) = g_{\rho NN}\bar{u}(p')\gamma_\mu u(p) \qquad (8)$$

$\tilde{V}_\mu^0$ is current source for J_μ. The bond of impulse conservation energy: $q = p' - p$ is between 4D impulses. Here p' and p are impulses before and after interaction between spinor and vector fields inside AdS space. p' and p are impulses of initial and final 4D nucleon in QSD theory. 5D interaction (1) characterizing the interaction between vector and fermion fields inside AdS space is used for calculation of interaction ρNN constant meson-nucleon. The expression of Langrangian interaction in an unfolded form should be given in (1). The given Langrangian expression is obtained according to calibration invariancy of the model used by us.

$$\mathcal{L}_{\rho NN}^{(0)} = \bar{N}_1 e_A^M \Gamma^A V_M N_1 + \bar{N}_2 e_A^M \Gamma^A V_M N_2. \qquad (9)$$

Here, N_1 and N_2 are 5D Dirac fermion fields and take under consideration the $SU(2)_L \times SU(2)_R$ chiral calibration group, they transform into (2,1) and (1,2). e_A^M being Weylbeyn transition from curvilinear space to rectilinear one, is defined by $e_M^A = \frac{1}{z}\eta_M^A$. V_M defines the vector field and Γ^A being the matrix of 5D Dirak fermion field, is defined by $\Gamma^A = (\gamma^\mu, -i\gamma^5)$.

$$\Gamma^5 = -i\gamma^5 = \begin{pmatrix} -i & 0 \\ 0 & i \end{pmatrix}, \Gamma^0 = \begin{pmatrix} 0 & -1 \\ -1 & 0 \end{pmatrix}, \Gamma^i = \begin{pmatrix} 0 & \sigma^i \\ -\sigma^i & 0 \end{pmatrix}, \text{(i=1,2,3)}.$$

Taking under consideration the current expression in (8), Langrangian interaction in (9) gives to the constant of $g_{\rho NN}$ meson-nucleon vector the following formula:

$$g_{\rho NN}^{(0)nm} = \int_0^{z_m} \frac{dz}{z^4} V_0(z)\left(f_{1L}^{(n)*}(z)f_{1L}^{(m)}(z) + f_{2L}^{(n)*}(z)f_{2L}^{(m)}(z)\right). \qquad (10)$$

$V_0(z) = (kz)^2\sqrt{2}L_0^{(1)}(k^2z^2)$ is profile function of Caluza-Klein mode vector field, $f_{1L}^{(n)}$ və $f_{1R}^{(m)}$ are nucleon profile functions. The profile functions for nucleons have been already given in equation (3). The spinors inside 5D AdS space have the magnetic moment. By this reason, they interact with vector field with the help of magnetic moment. According to this interaction, Langrangian is obtained by 4D theory and has the following form:

$$\mathcal{L}_{FNN}^{(1)} = ik_1 e_A^M e_B^N (\bar{N}_1 \Gamma^{AB}(F_L)_{MN} N_1 - \bar{N}_2 \Gamma^{AB}(F_R)_{MN}N_2) \quad (11)$$

Here, i is a complex unit, k_1 is constant coefficient, e_A^M and e_B^N being вeing Weyl bey transition from curvilinear space to rectilinear one, is defined by $e_M^A = \frac{1}{z}\eta_M^A$. N_1 and N_2 are 5D Dirac fermion fields. $\Gamma^{MN}F_{MN}$ matrixes consist of the sum of two boundaries $F^{5v}F_{5v}$ and $\Gamma^{\mu v}F_{\mu v}$. Using Langrangian interaction $L_{FNN}^{(1)}$, gives to the constant of $g_{\rho NN}$ meson-nucleon vector the following formula:

$$g_{\rho NN}^{(1)nm} = -2\int_0^\infty \frac{dz}{z^3} e^{-k^2z^2} \grave{V}_0(z)[k_1\left(f_{1L}^{(n)*}(z)f_{1L}^{(m)}(z) - f_{2L}^{(n)*}(z)f_{2L}^{(m)}(z)\right) + k_2 v(z)\left(f_{1L}^{(n)*}(z)f_{2L}^{(m)}(z) + f_{2L}^{(n)*}(z)f_{1L}^{(m)}(z)\right)]. \qquad (12)$$

NUMERICAL CALCULATIONS

Thus, two integral expressions (10) and (12) are obtained in AdS/QSD hard wall model for $g_{\rho NN}$ interaction constant of ρ meson-nucleon. The final interaction constant is the sum of two expressions:

$$g_{\rho NN}^{s.d.} = g_{\rho NN}^{(0)nm} + g_{\rho NN}^{(1)nm}. \qquad (13)$$

The unit calculations (13) are calculated with the help of MATHEMATICA program. $a = 0.2757$ is calculated for A constant in $SU(2)$ symmetry. The following units: m_n=0.94 (GeV), $\sigma =(0.213)^3$ GeV^3, m$_q$=0.0083 GeV, k$_1$=-0.98 GeV^3, $k_2 = 0.5$ GeV^3 are used for parameter sum. Taking under consideration these constant values we obtain the final calculation $g_{\rho NN}^{s.d.}$ =0,078.

[1] *A. Cherman, T.D. Cohen, E.S. Werbos.* Phys. Rev. C79, 2009, 045203.
[2] *Makoto Natsuume.* ADS/CFT Duality User Guide, Lecture Notes in Physics 903, Springer.
[3] *D.K. Hong, T. Inami and H.U. Yee.* Physics Letters B646:165-171, 2007.
[4] *H.C. Ahn. D.K. Hong, C.Park and S. Siwach.* Physics Review D 80, 2009, 054001.
[5] *H.R. Grigoryan and A.V. Radyushkin.* Physics Review D 76, 2007, 095007.

[6] *J. Erlich, E. Katz, D.T. Son and M.A. Stephanov.* Physics Review Letters 95:261602, 2005.
[7] *N.Huseynova, Sh. Mamedov.* Int. J.Th. Phy. 2015, № 54, pp. 3799-3810
[8] *N. Maru and M. Tachibana.* Eur. Phys. J. C, 2009, v.63, pp. 123-132.
[9] *Z. Abidin and C. Carlson.* Phys. Rev.D79, 2009, 115003.
[10] *A. Karch, E.Katz, D.T.Son and M.A. Stephanov.* Physics Review D 74, 2006, 015005.

CONTENTS